Programmable Quantum Matter: Heralding Large Cluster States in Driven Inhomogeneous Spin Ensembles

Pratyush Anand,[1,2,*] Louis Follet,[1,2,*] Odiel Hooybergs,[1,2,3,4,*] and Dirk R. Englund[1,2,†]

[1] *Department of Electrical Engineering and Computer Science, Massachusetts Institute of Technology, Cambridge, Massachusetts 02139, USA*

[2] *Research Laboratory of Electronics, Massachusetts Institute of Technology, Cambridge, Massachusetts 02139, USA*

[3] *Department of Physics, ETH Zürich, Zürich 8093, Switzerland*

[4] *Quantum Center, ETH Zürich, Zürich 8093, Switzerland*

(Received 12 September 2025; accepted 6 May 2026; published 16 June 2026)

Atom-like emitters in solids have emerged as promising platforms for quantum sensing and information processing. Among the major challenges are inhomogeneities in emitter fine structure, which complicates quantum control. Here, we introduce a framework that leverages this emitter diversity to simplify the experimental resources needed to create optically heralded spin cluster states across N_q emitters from the conventional order $O(N_q)$ to $O(1)$ within ensembles of $N_q \sim 10$–100. Specifically, the optimized pulse sequence simultaneously corrects parameter variations (pulse-length error and frequency detuning error), achieving single-qubit gate fidelities exceeding 99.99% for errors (normalized relative to Rabi-drive strength) up to 0.3, while maintaining fidelities above 99% even for errors as large as 0.4. Applying this optimized pulse sequence in the form of a Carr-Purcell-Meiboom-Gill (CPMG) based dynamical decoupling protocol to the dominant noise spectral density of silicon-vacancy centers in diamond, our approach enhances ensemble-average coherence times by more than a factor of 7 relative to interleaved bang-bang-based CPMG. For state-of-the-art dilution refrigeration systems, we further estimate sharply reduced heating when driving a global resonant optimal dynamical decoupling across N_q silicon-vacancy spins, potentially resolving the current trade-off between spin coherence and scaling to $N_q \gg 1$. We further introduce a modified single-photon entanglement protocol with an efficient algorithm for deterministic entanglement compilation. Depending on the decoupling window, our method yields order $O(10^2$–$10^4)$ more entanglement links than bang-bang sequences, with theoretical guarantees of order $\Omega(N_q)$ unique links—improvable via control-parameter tuning. Our approach thus offers enhanced fidelity, scalability, and robustness. Together, these techniques provide foundational tools—including global unitary control, phase denoising, remote entanglement, and compilation—for scalable quantum computing architectures based on heterogeneous spin ensembles.

DOI: 10.1103/kb8s-sffj

I. INTRODUCTION

Among atom-like emitters, diamond color centers now support high-coherence spin-photon interfaces and optically heralded remote entanglement [1–7]. Building on the quantum network milestones and recent modular frameworks for photon-mediated entanglement, these platforms provide a concrete path toward programmable quantum network nodes [1,8–14]. Scaling such nodes imposes several key requirements: spin coherence must be preserved throughout repeated, probabilistic optical attempts, necessitating dynamical decoupling that remains effective across heterogeneous ensembles (*R1*); control must be uniform and high fidelity, both single- and two-qubit gates should tolerate amplitude and detuning variations with minimal per-emitter calibration (*R2*) [15]; optically heralded entanglement must produce indistinguishable photons while protecting the memory state, as in single-photon or Barrett-Kok-type protocols (*R3*) [8,9,12,16]; compilation and scheduling should orchestrate many entanglement attempts in parallel with guarantees on link count and uniqueness (*R4*) [11,17–21]; all of the above requirements

*These authors contributed equally to this work.

†Contact author: englund@mit.edu

Published by the American Physical Society under the terms of the Creative Commons Attribution 4.0 International license. Further distribution of this work must maintain attribution to the author(s) and the published article's title, journal citation, and DOI.

must be thermally feasible within cryogenic power budgets during extended control and decoupling windows (*R5*) [22].

Today's implementations fall short on several fronts. Standard bang-bang (CPMG/XY) decoupling [24] is detuning-sensitive and relies on high peak power, leading to rapid performance loss and heating in inhomogeneous ensembles. For the number of qubits being N_q, per-emitter interleaving of controls scales as order $O(N_q)$, compressing interpulse spacings below thermalization times and eroding T_2 and T_2^* [2,25]. Entanglement scheduling via optical switching introduces insertion loss and synchronization complexity that directly suppress heralding rates, while photon-frequency inhomogeneity often forces filtering or matching that further reduces throughput unless compensated at the control level.

Here, we replace lossy optical-switch scheduling with *resonant, composite drive engineering*. A single optimized waveform provides global unitary control and dynamical decoupling across heterogeneous emitters—reducing control overhead from $O(N_q)$ to $O(1)$—while maintaining high fidelity under detuning spread and lowering thermal load. Combined with a deterministic entanglement compiler, this enables optically heralded links with orders-of-magnitude higher throughput and guaranteed coverage.

As seen from Fig. 1 we propose to use two spatially separated spin ensembles to create a bipartite cluster state which acts as a resource for measurement-based quantum computing [26,27]. This state is set of entanglement links $\{j-k\}$ where j,k are qubit labelings in devices $\mathcal{M}_A$ and $\mathcal{M}_B$ respectively. This approach, however, transforms the challenge from a simple entanglement generation and scheduling [19,28,29] limitation into a complex, multiparameter optimization problem. The central task becomes minimizing the global cost function $J(\theta)$, defined as the average two-qubit error over all generated links,

$$J(\theta) = \left\langle \epsilon_{jk}(\theta) \right\rangle_{j,k}. \tag{1}$$

Optimization is performed on the vector of experimental parameters $\theta = \{P_{\text{pulse}}, P_{\text{DDS}}, P_{\text{comp}}\}$, which includes the temporal shape of control pulses, the architecture of the dynamical decoupling sequences [24,30], and the scheduling of entanglement attempts respectively. The error for each link, ϵ_{jk}, is a function of both coherent control errors and decoherence during the entanglement protocol, as detailed in Eq. (26). Crucially, the fidelity decoherence

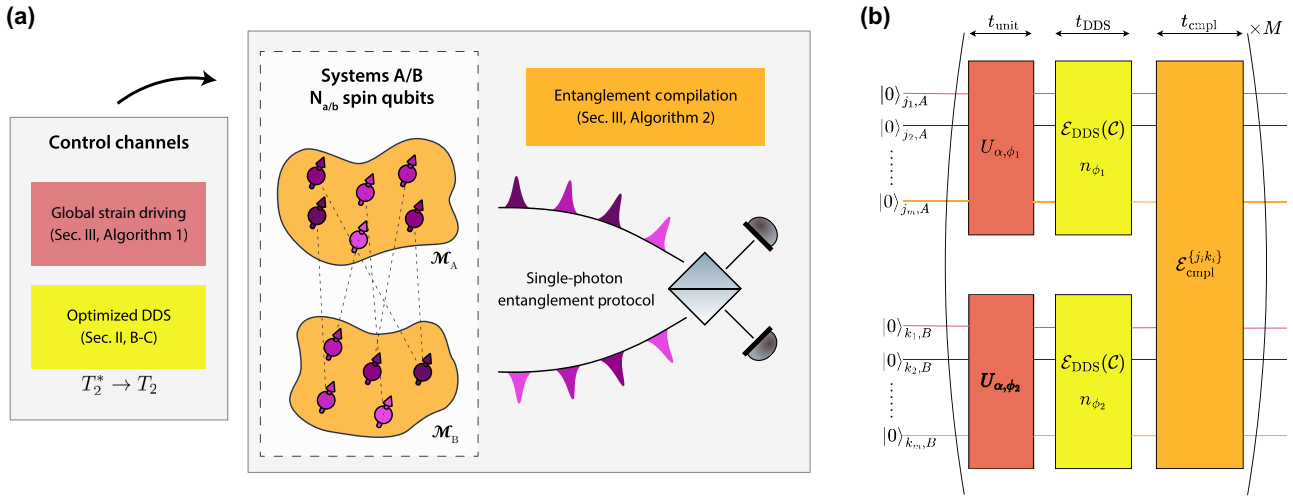


FIG. 1. Architecture and protocol for mechanical bipartite-graph cluster-state generation. (a) Architecture overview. Devices $\mathcal{M}_{A/B}$ (Systems A/B, $N_{a,b}$ spin qubits) are arbitrary mechanical structures that house heterogeneous color-center ensembles with nonuniform spin frequencies and spin-strain susceptibilities (represented by arbitrary color shades), operating in noisy environments. Each ensemble is controlled by a single global strain drive that provides programmable qubit addressing (Sec. III, Algorithm 1) and is operated with optimized dynamical decoupling sequences (Secs. II B and II C), yielding robust quantum operations and extended spin coherence. A single-photon entanglement protocol generates heralded Bell pairs between the two ensembles; these pairs are compiled (Sec. III, Algorithm 2) into a two-dimensional bipartite-graph cluster state. For clarity, only a representative subset of entanglement links is shown with dashed lines. (b) Quantum circuit diagram of the full protocol. The protocol starts with two sets of qubits in systems A and B respectively: $\{|0\rangle_{j_i,A}\}, \{|0\rangle_{k_i,B}\}$ initialized in their respective ground states. A global initialization unitary $U_{\alpha,\phi_{1,2}}$ (in red) of time duration t_{unit} prepares the initial state in a coherent superposition. Further, the global dynamical decoupling channel $\mathcal{E}_{\text{DDS}}$ (in yellow) reduces the phase noise of the systems, taking a time of t_{dds}. After this step, the compiler schedules pair-wise entanglement in the sequence: $\{(j_i, k_i)\}$, represented by the block $\mathcal{E}_{\text{cmpl}}$ (in orange) which takes time t_{cmpl}. The whole block is repeated for M attempts to increase the success rate of entanglement. The inner architecture of these blocks are described in detail in Sec. III in the Supplemental Material [23].

for each link is determined by the compilation strategy P_{comp}, which demands an efficient compilation strategy to build a graph state in PSPACE [31] and polynomial time. The value of $J(\theta)$ is therefore determined by the interplay between single-qubit gate fidelities, thermally limited coherence times, and the probabilistic efficiency of the underlying single-photon entanglement protocol [16]. Our work systematically deconstructs and optimizes the components of $J(\theta)$ to deliver a scalable and robust solution.

To solve this optimization problem, we take advantage of the diversity of color centers. This inherent heterogeneity provides the unique spectral labels necessary for qubit addressability under a global drive, which resolves the challenge of scheduling remote entanglement attempts that would otherwise scale super-exponentially. Our integrated approach, summarized in Fig. 1, therefore delivers four key components: (i) high-fidelity global unitary control (*R2*, *R5*), (ii) broadband dynamical decoupling (*R1*, *R2*), (iii) a single-photon remote entanglement protocol (*R3*), and (iv) an efficient compilation algorithm to generate a bipartite cluster state [32] (*R4*).

We illustrate it on diamond-based group-IV defect centers [33–39], specifically the negatively charged silicon-vacancy center (SiV^-) which are optically active [2,40,41] and feature addressable—via microwave or mechanical strain—electronic spin states [42,43] (serving as control qubits) and nearby nuclear spin states [13,44] (serving as memory qubits). These defect centers have been previously demonstrated as a quantum network node [13,14,45], single photon sources [46,47] (serving as communication qubits), and have also been proposed for blind quantum computing [48]. Having a well-studied [43] strain dependence of its qubit characteristics makes this substrate programmable up to device constraints. Therefore, the SiV^- center contains all the major components required by a quantum computational substrate in our proposed framework.

In Sec. II, we introduce the system architecture: an ensemble of SiV^- centers driven by a global mechanical signal. We first establish the strain-mediated control of single-qubit gates (Sec. II A). To overcome the ensemble's spectral inhomogeneity, we implement simultaneous amplitude and frequency error-correcting gradient ascent pulse engineering (SAFE-GRAPE) (Sec. II B), a modified optimization routine that synthesizes control pulses robust to simultaneous amplitude and detuning errors [49,50]. A single drive can effectively control our ensemble in a coherent way, forming a state of driven matter. These global operators enable simultaneous dynamical decoupling across the ensemble, substituting the rapid decoherence time T_2^* with the extended T_2. In Sec. II C, we quantify this performance via filter-function analysis, contrasting our spectrally adapted sequences against conventional bang-bang Carr-Purcell-Meiboom-Gill (CPMG) protocols [51,52]. Section III extends this framework to quantum computation, developing a formalism for bipartite cluster-state generation via single-photon entanglement. We utilize a statistical quantum volume definition [53] to demonstrate the architectural superiority of SAFE-GRAPE over standard methods, concluding with a deterministic compilation algorithm for graph state assembly.

II. THEORETICAL FRAMEWORK

A. System description

Consider a set of N_q group-IV color centers in diamond. The ground states (GSs) and excited states (ESs) manifold of each color center CC_i are described by the Hamiltonian $\hat{\mathcal{H}}_i^{\text{GS/ES}}$ that includes the strain, spin-orbit (SO), and Zeeman interaction,

$$\hat{\mathcal{H}}_i^{\text{GS/ES}} = \hat{\mathcal{H}}_i^{\text{strain}} + \hat{\mathcal{H}}_i^{\text{SO(GS/ES)}} + \hat{\mathcal{H}}_i^{\text{Zeeman}}. \tag{2}$$

While our protocol is generally applicable to group-IV color centers due to their shared D_{3d} symmetry, we illustrate it using the transverse-oriented SiV^- center as a well-characterized model system. Its explicit Hamiltonian, which accounts for the defect's orbital structure and its interaction with the magnetic field and lattice strain, is detailed in Sec. I.A in the Supplemental Material [23].

Let us focus on the GS manifold and use its bottom two energy levels as a qubit with energy spacing $\hbar\omega_i$. An arbitrary single-qubit gate of type $\hat{\mathcal{U}}^{\text{ideal}}(\theta,\phi) = \exp\{-i(\theta/2)(\cos\phi\hat{\sigma}_x + \sin\phi\hat{\sigma}_y)\}$ can be implemented using the strain-driving Hamiltonian $\hat{\mathcal{H}}_i^{\text{drive}}$ [43],

$$\hat{\mathcal{H}}_i^{\text{drive}} = \begin{bmatrix} 0 & 0 & \epsilon^{ac}_{E_{gx},i} & 0 \\ 0 & 0 & 0 & \epsilon^{ac}_{E_{gx},i} \\ \epsilon^{ac}_{E_{gx},i} & 0 & 0 & 0 \\ 0 & \epsilon^{ac}_{E_{gx},i} & 0 & 0 \end{bmatrix} \cos(\omega_d t_i + \varphi). \tag{3}$$

The strain oscillations are driven at frequency ω_d and phase offset φ, where these are chosen to satisfy $\omega_d = \omega_i$ and $\varphi = \pi - \phi$. The evolution time t_i should be picked equal to θ/Ω_i. The effective Rabi frequency Ω_i is determined by fitting a squared sinusoid to the probability of finding the color center in its ground state after initialization in the first excited state. Further details on the realization of strain-driven arbitrary single-qubit gates are provided in Sec. I.B in the Supplemental Material [23].

In our framework we are using a global strain drive, i.e. strain pulses that act on all N_q color centers. Hence, the strain drive frequency is detuned differently from all color centers: $\omega_d = \omega_i + \Delta_i$. This occurs due to different local strain environments $\epsilon^{dc}_{E_{gx},i}$. Furthermore, the effective Rabi frequency can vary for all color centers: $\Omega_i = \Omega(1+\epsilon_i)$.

These variations encompass two effects: different strain modulation amplitudes $\epsilon^{ac}_{E_{gx},i}$ due to different locations in the device and different spin-strain susceptibilities for different local strain environments. As a result, the dynamic evolution for a time $t = \theta/\Omega$ of each color center i under $\hat{\mathcal{H}}^{\text{drive}}_i$ is given by the unitary operator $\hat{\mathcal{U}}^{\text{real}}_{\epsilon_i,f_i}(\theta,\phi)$,

$$\hat{\mathcal{U}}^{\text{real}}_{\epsilon_i,f_i}(\theta,\phi) = \exp\left\{-\frac{i}{\hbar}\hat{\mathcal{H}}^{\text{drive}}_i t\right\}$$
$$\cong \exp\left\{-i\frac{\theta}{2}[(1+\epsilon_i)(\cos\phi\hat{\sigma}_{x,i} + \sin\phi\hat{\sigma}_{y,i}) - if_i\hat{\sigma}_{z,i}]\right\}.$$

Here $\cong$ denotes the corresponding action on the bottom two energy levels. By comparing $\hat{\mathcal{U}}^{\text{real}}_{\epsilon_i,f_i}(\theta,\phi)$ with $\hat{\mathcal{U}}^{\text{ideal}}(\theta,\phi)$ it is clear that each color center experiences an amplitude error ϵ_i and an off-resonance error $f_i = \Delta_i/\Omega$.

The total system Hamiltonian for our set of N_q color centers and global strain drive is given by

$$\hat{\mathcal{H}}^{\text{total}} = \sum_{i=1}^{N_q}\left(\hat{\mathcal{H}}^{\text{GS}}_i + \hat{\mathcal{H}}^{\text{drive}}_i\right). \tag{4}$$

B. Error-correcting pulses

1. Composite pulses

The application of a single strain pulse to a set of N_q color centers introduces systematic control errors $\{\epsilon_i,f_i\}_{i\in[1\cdots N_q]}$. To mitigate these errors, robust pulse sequences from the nuclear magnetic resonance field are adapted. Composite pulses, denoted as $\hat{\mathcal{U}}_{CP}(\theta,\phi)$, are constructed as sequences of elementary single-qubit gates $\hat{\mathcal{U}}(\theta_i,\phi_i)$,

$$\hat{\mathcal{U}}_{CP}(\theta,\phi) = \prod_{i=1}^{N_p}\hat{\mathcal{U}}(\theta_i,\phi_i), \tag{5}$$

where N_p is the number of pulses in the sequence. Specifically, the BB1 sequence [54] addresses amplitude errors, while CORPSE [55] mitigates off-resonance errors. For simultaneous robustness against both errors, we employ the reduced CinBB (inner pulse is CORPSE, and outer pulse is BB1 (Broadband composite pulse) (rCinBB) pulse [56], a concatenated composite pulse integrating CORPSE within the BB1 framework (see Sec. II.B in the Supplemental Material [23]). The operator for the rCinBB pulse is expressed as $\hat{\mathcal{U}}_{rCinBB}(\theta,\phi) = \prod_{i=1}^{6}\hat{\mathcal{U}}(\theta_i,\phi_i)$, with parameters given in Table S2 in the Supplemental Material [23].

2. SAFE-GRAPE

More accurate error mitigation can be achieved by SAFE-GRAPE of composite pulses. Define the composite search space $\mathbf{\Omega}$ as the region of errors that should be mitigated, e.g. $\mathbf{\Omega} = \{(\epsilon,f)|\epsilon_{\min} < \epsilon < \epsilon_{\max} \wedge f_{\min} < f < f_{\max}\}$. The goal is to find a set $\{\theta_i,\phi_i\}_{i\in[1\cdots N_p]}$ such that

$$\forall(\epsilon,f)\in\mathbf{\Omega} : \prod_{i=1}^{N_p}\hat{\mathcal{U}}^{\text{real}}_{\epsilon,f}(\theta_i,\phi_i) \approx \hat{\mathcal{U}}^{\text{ideal}}(\theta,\phi). \tag{6}$$

The SAFE-GRAPE algorithm discretizes $\mathbf{\Omega}$ to $\mathbf{\Omega}^*$, e.g. $\mathbf{\Omega^*} = \{\underbrace{\epsilon_{\min},\ldots,\epsilon_{\max}}_{N_\epsilon}\} \times \{\underbrace{f_{\min},\ldots,f_{\max}}_{N_f}\}$. For each point in the discretized composite search space, we calculate the average gate infidelity $1-\overline{\mathcal{F}}(\epsilon,f)$ between the composite-pulse sequence and the target operation. The SAFE-GRAPE algorithm then minimizes the total loss function $\mathcal{L}$, which is given by

$$\mathcal{L} = \sum_{(\epsilon,f)\in\mathbf{\Omega^*}} \underbrace{\left[1 - \frac{1}{2}\text{Tr}\left[\left(\hat{\mathcal{U}}^{\text{ideal}}(\theta,\phi)\right)^\dagger \prod_{i=1}^{N_p}\hat{\mathcal{U}}^{\text{real}}_{\epsilon,f}(\theta_i,\phi_i)\right]\right]}_{1-\overline{\mathcal{F}}(\epsilon,f)} \mathcal{W}(\epsilon,f), \tag{7}$$

where we introduced the additional weight factor $\mathcal{W}(\epsilon,f)$. If all the points in the composite search space are equally important, $\mathcal{W}(\epsilon,f) = 1$ is a good choice. Alternatively, the center $(\bar{\epsilon},\bar{f})$ of the composite search space can be prioritized using a Gaussian weight factor $\mathcal{W}(\epsilon,f) = \mathcal{N}\exp\left(-((\epsilon-\bar{\epsilon})^2/2\sigma_\epsilon^2) - (f-\bar{f})^2/2\sigma_f^2\right)$, with the appropriate normalization constant $\mathcal{N}$.

At the start of the SAFE-GRAPE algorithm we define the hyperparameters of the model. θ and ϕ define the target unitary $\hat{\mathcal{U}}^{\text{ideal}}(\theta,\phi)$. By selecting different values for θ and ϕ it is possible to implement an arbitrary single-qubit gate. N_p sets the number of pulses in the composite-pulse sequence. $\epsilon_{\min},\epsilon_{\max},N_\epsilon,f_{\min},f_{\max}$, and N_f define the discretized composite search space $\mathbf{\Omega^*}$. The

relative importance of points within $\mathbf{\Omega^*}$ is set by the definition of $\mathcal{W}(\epsilon,f)$. The effective Rabi-drive strength Ω is fixed, so all off-resonance errors f_i are constant for the respective color centers with fixed detuning Δ_i. Since $t=\theta/\Omega$, we can now represent the composite pulse sequence $\prod_{i=1}^{N_p}\hat{\mathcal{U}}^{\text{real}}_{\epsilon,f}(\theta_i,\phi_i)$ by the set of trainable parameters $\{t_i,\phi_i\}_{i\in[1\cdots N_p]}$. These are initialized based on the rCinBB composite-pulse sequence. We use a sigmoid reparametrization in order to force each t_i to lie in $[t_{\min},t_{\max}]$, where $t_{\min}$ and $t_{\max}$ are also hyperparameters of the model,

$$t_i \to \tilde{t}_i = t_{\min} + (t_{\max}-t_{\min})\frac{1}{1+\exp(-t_i)}. \tag{8}$$

We implement the SAFE-GRAPE algorithm in `PyTorch` [57] and use the built-in L-BFGS optimizer [58]. Section II.C in the Supplemental Material [23] lists all the parameter values used in the SAFE-GRAPE algorithm.

As an example, we implement SAFE-GRAPE for a π-X gate $\hat{\mathcal{U}}^{\text{ideal}}(\theta=\pi,\phi=0)$. The resulting optimal control pulse sequence is shown and compared to the rCinBB pulse sequence in Fig. 2(a). To illustrate the effect of both pulse sequences, we show their action on the ground state in Fig. 2(c). When no amplitude error or off-resonance error is present, both rCinBB and SAFE-GRAPE perform well, achieving a fidelity of 100% and >99.999% respectively. Once amplitude and off-resonance errors are introduced, rCinBB fidelity decreases more rapidly. In the case of $\epsilon=f=0.25$, the respective fidelities drop to 92.7% and 99.987%. SAFE-GRAPE still manages to flip the initial $|0\rangle$ state close to the $|1\rangle$ state on the Bloch sphere, whereas for rCinBB the yellow arrow indicating the final state is clearly deviating from the $|1\rangle$ state. Hence, at the cost of higher bandwidth requirements and a 51% increase in pulse duration with respect to the rCinBB pulse sequence, SAFE-GRAPE produces a more robust pulse with $<10^{-4}$ average gate infidelity for most of the composite search area [Fig. 2(b)].

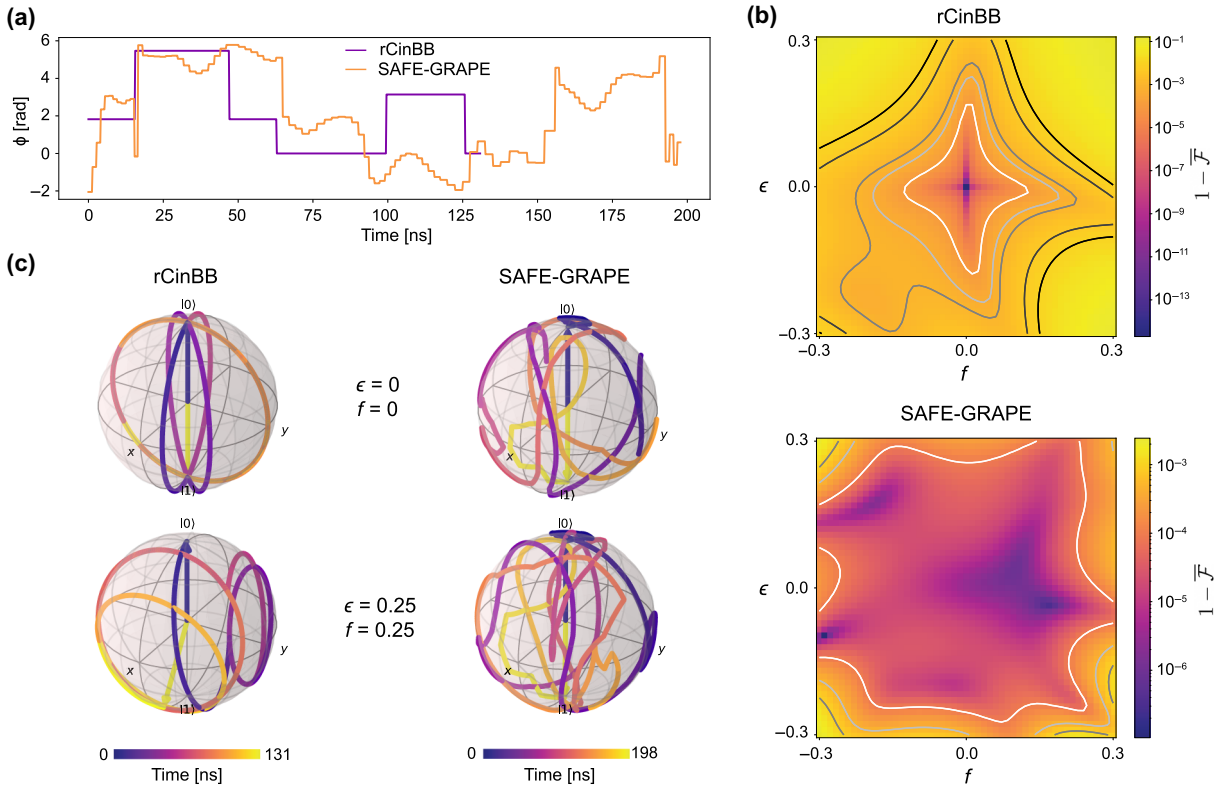


FIG. 2. Simultaneous amplitude and frequency error-correcting gradient ascent pulse engineering optimal control pulse sequence for implementing $\hat{\mathcal{U}}^{\text{ideal}}(\theta=\pi,\phi=0)$. (a) Control pulse sequence before (reduced CinBB) and after (simultaneous amplitude and frequency error-correcting gradient ascent pulse engineering) optimization for a Rabi-drive strength $\Omega=200$ Mrad/s. (b) Average gate infidelity heatmap for reduced CinBB (top) and simultaneous amplitude and frequency error-correcting gradient ascent pulse engineering (bottom) pulse sequence. Contours denote infidelities of $10^{-4}, 5\times10^{-4}, 10^{-3}, 5\times10^{-3}$ and 10^{-2}, increasing from white to black. Note that both plots have their own color bar. (c) Action of reduced CinBB (left) and simultaneous amplitude and frequency error-correcting gradient ascent pulse engineering (right) pulse sequence on the Bloch sphere for initial state $|0\rangle$ in case of $\epsilon=f=0$ (top) and $\epsilon=f=0.25$ (bottom). On each Bloch sphere, the purple and yellow arrows point at the initial and final state respectively.

In Fig. 2(b), we vary normalized amplitude and detuning errors $(\epsilon, f) \in [-0.3, 0.3]$, where $f \equiv \Delta/\Omega_0$ is the detuning normalized to the nominal Rabi rate Ω_0. Thus the ± 0.3 range is intended to capture experimentally relevant, MHz-scale residual variations during spin control (after standard resonance identification and/or coarse tuning), rather than the full GHz-scale static inhomogeneity across an untreated SiV ensemble. The SiV spin transition depends strongly on local strain [43], leading to center-frequency differences across distinct emitters that can be GHz-scale. In practice, coherent control is typically performed on a selected set of SiVs (a narrow spectral class) after calibrating its resonance; the remaining detuning during operation is then dominated by drift and dephasing-related fluctuations on the scale of a few MHz to $\sim 10\,\mathrm{MHz}$ (consistent with typical T_2^* and measured spin-resonance linewidths [42]). For our nominal $\Omega_0 = 2\pi \times 30\,\mathrm{MHz}$, $|f| \leq 0.3$ corresponds to $|\Delta| \leq 0.3\,\Omega_0 \approx 2\pi \times 9\,\mathrm{MHz}$, which provides a realistic robustness margin against these residual detunings. We choose a $\pm 30\%$ amplitude error to ensure robustness to large Rabi-drive fluctuations arising from (i) spatial variation of strain-wave amplitude across the device, (ii) center-to-center differences in spin-strain susceptibility due to static strain [43], and (iii) minor microwave power instability.

The average gate infidelity represents the fidelity between the state after evolution by the composite-pulse sequence and the target final state, averaged over all possible input states. Here we have calculated the fidelity based on perfect control pulses, such that the resulting infidelity maps reflect best the differences between the two composite control pulse sequences.

In the Supplemental Material [23] we also introduce bandwidth-aware SAFE-GRAPE. It is an adapted version of the algorithm that allows one to restrict the bandwidth of the optimal control pulse so that it is compatible with specific experimental hardware. We show that we can find an optimal control pulse for an I/Q drive with a bandwidth of 100 MHz that is able to achieve similar infidelities as the control pulse in Fig. 2 over the same composite search space.

C. Dynamical decoupling: Frequency domain picture

In the previous section, we talked about a GRAPE-based composite-pulse sequence to implement a π rotation which corrects both off-resonance errors and amplitude errors. Correcting these errors ensures that all the qubits in the ensemble experience the same π pulse upto a given fidelity as seen from the heat-map in Fig. 2. We propose to concatenate this optimized pulse for many cycles to implement a dynamical decoupling sequence on all qubits simultaneously. In order to quantify these sequences, we use the filter-function formalism [59], and thereby estimate the enhancement in T_2 time of the system of qubits.

In the presence of a decohering environment, the Hamiltonian in Eq. 4, changes to

$$\hat{\mathcal{H}}^{\text{total}} = \sum_{i=1}^{N_q} \left(\hat{\mathcal{H}}_i^{\text{GS}} + \hat{\mathcal{H}}_i^{\text{drive}} + \hat{\mathcal{H}}_i^{\text{noise}} \right), \tag{9}$$

where $\hat{\mathcal{H}}_i^{\text{noise}}$ is given by [60,61]

$$\hat{\mathcal{H}}_i^{\text{noise}} = \sum_k s_{k,i}(t) b_{k,i}(t) \hat{\mathbf{B}}_{k,i}. \tag{10}$$

Here $\hat{\mathbf{B}}_{k,i}$ is the set of noise operators via which qubit i couples to the environment, $b_{k,i}(t)$ is the classically fluctuating noise variable for qubit i and noise mode k, $s_{k,i}(t)$ is the deterministic time-dependent sensitivity for the noise operator $\hat{\mathbf{B}}_{k,i}$. In order to simplify our analysis, we assume that the qubit ensemble only experiences dephasing noise (i.e. $k = 1$, $\hat{\mathbf{B}}_i = \hat{\sigma}_{z,i}$) and we further assume that the noise mode is always coupled to the qubit with a constant sensitivity s_i, which can be absorbed in the noise variable $b_i(t)$. For the filter-function formalism, we consider the power spectral density of the fluctuating variables given by

$$\mathcal{S}_i(\omega) = \int_0^\infty e^{-j\omega\tau} \langle b_i(t+\tau) b_i(t) \rangle \, \mathrm{d}\tau. \tag{11}$$

Furthermore, we define the coherence of the ith qubit spin state after time τ as [59]

$$W_i(\tau) = |\overline{\langle \sigma_{y,i} \rangle}| \equiv e^{-\chi_i(\tau)}. \tag{12}$$

Here the angled brackets represent the quantum-mechanical expectation value and the overline represents the average over multiple measurement outcomes on qubit i. Using these definitions, we have the following relation [59]:

$$\chi_{ij}(\tau) = \frac{2}{\pi} \int_0^\infty \frac{\mathcal{S}_i(\omega)}{\omega^2} F_{ij}(\omega\tau) \, d\omega. \tag{13}$$

We introduce the filter function (spectral dependence) $F_{ij}(\omega\tau)$ of the experiment sequence j being performed on qubit i, which in our case will be a dynamical decoupling sequence. We further represent $\chi(\tau)$ as follows:

$$\chi_{ij}(\tau) \equiv \left(\frac{\tau}{T_{2,ij}} \right)^{z_{ij}}, \tag{14}$$

where $T_{2,ij}$ is the coherence time of qubit i, after implementing an experimental sequence j, and z_{ij} is the corresponding scaling, which depends on the noise spectrum $\mathcal{S}_i$. We further simplify our analysis by assuming that all qubits experience the same noise spectrum and are

equally sensitive [i.e. $s_i = s$, $\mathcal{S}_i(\omega) = \mathcal{S}(\omega)\ \forall\ i$]. We consider a double-exponential noise spectrum as seen in the Supplemental Material of SiV^- paper [2],

$$\mathcal{S}(\omega) = c_0 e^{-\omega^2/\omega_0^2} + c_1 e^{-\omega^2/\omega_1^2}, \tag{15}$$

where we assume the same values from the paper: $c_0 = 10^6\,\mathrm{s}^{-1}$, $c_1 = 10^9\,\mathrm{s}^{-1}$, $\omega_0 = 1.8\times10^3\,\mathrm{s}^{-1}$, $\omega_1 = 50\,\mathrm{s}^{-1}$. For the composite-pulse sequence generated by optimizing the cost function $\mathcal{L}$ in Eq. (8), we numerically evaluate the filter function using the `filter_function` package [62] available in `Python`.

For the comparison, we consider two sequence forms [Fig. 3(a)]: $\{\mathcal{A}_i(\tau), \mathcal{B}_i(\tau, m)\}$ for $i \in \{2, 4, 8, 16\}$, where the sequence $\mathcal{A}_i(\tau)$ is composed of i cycles of SAFE-GRAPE optimized pulses uniformly spaced over a measurement window τ, and $\mathcal{B}_i(\tau, m)$ represents the m-times (addressing m qubits individually) concatenated CPMG sequence with i cycles over the measurement window τ in the bang-bang regime.

We note that in our simulated inhomogeneous ensemble, the frequency separation between emitters is smaller than the Rabi frequency. In a standard experimental setup, this would inevitably lead to significant crosstalk for sequence $\mathcal{B}$ if individual addressing were attempted. However, we deliberately excluded crosstalk effects from the simulation of sequence $\mathcal{B}$ to construct a *steelman* baseline (an idealized upper bound) for comparison. By assuming that sequence $\mathcal{B}$ operates with perfect crosstalk mitigation strategies (e.g. via advanced methods like spatial selection or strong B-field gradients), we grant the baseline performance level that is physically optimistic and likely unattainable in practice.

Figure 3(b) shows the numerically simulated filter functions F_{ij}/ω^2 versus $\omega\tau$ on a log-log scale for sequences $\mathcal{A}_N$, where N is the number of π pulses for $\epsilon = f = 0$. As N increases from 1 to 32, the low-frequency part of the filter (e.g. $\omega\tau \lesssim 10$) is increasingly suppressed, with filter values dropping by over 7 orders of magnitude—from around 10^{-5} for $\mathcal{A}_1$ to below 10^{-12} for $\mathcal{A}_{32}$. Strong oscillations appear in the range $\omega\tau \sim 10^2$ to 10^6, becoming denser and

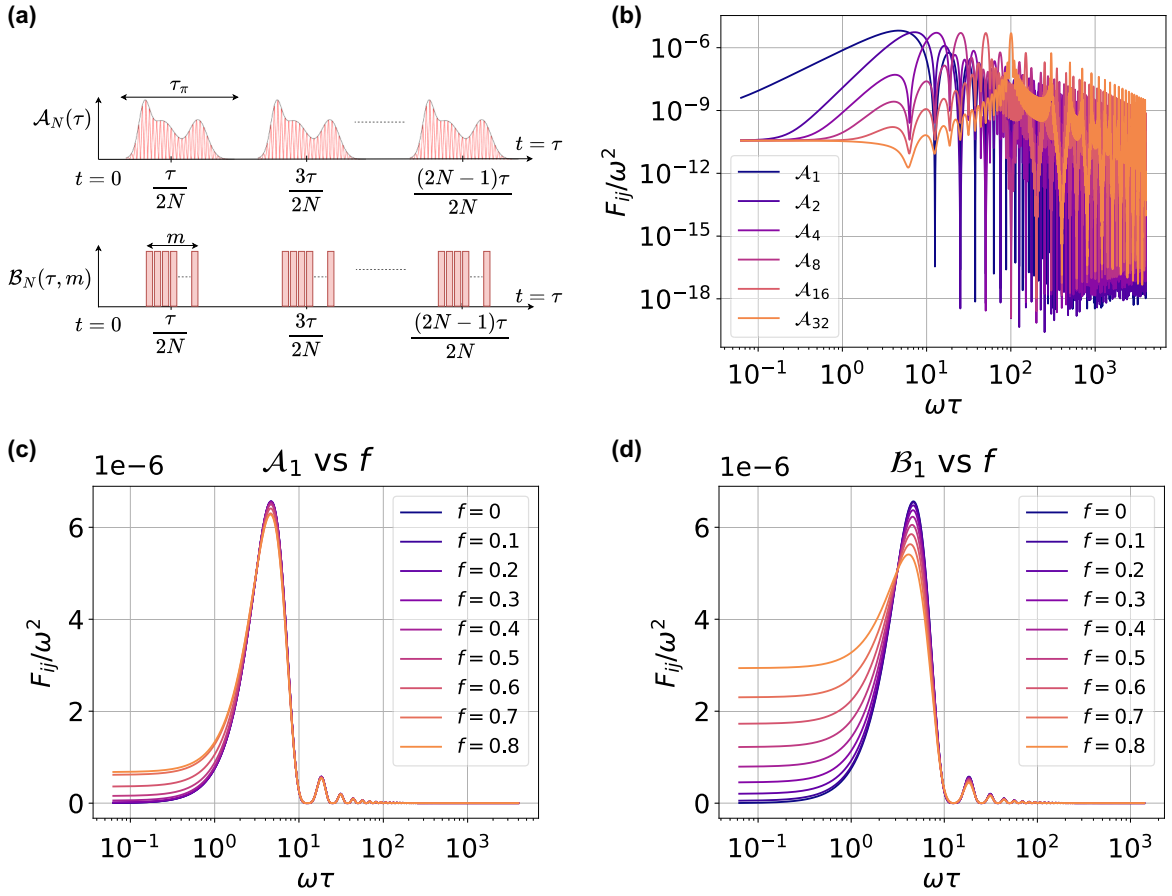


FIG. 3. Filter-function simulations. (a) Schematic for sequences $\mathcal{A}_N(\tau)$ and $\mathcal{B}_N(\tau, m)$. (b) As N increases, the modified filter function F_{ij}/ω^2 for $\mathcal{A}_N$ reduces, representing increased noise suppression. (c) F_{ij}/ω^2 for $\mathcal{A}_1$ rises for increased pulse detuning f. (d) There is a much larger increment in F_{ij}/ω^2 for $\mathcal{B}_1(m=1)$ for the same change in f. This shows that sequence $\mathcal{A}_N$ is more robust against off-resonance errors and hence better for implementing a dynamical decoupling sequence than sequence $\mathcal{B}_N$ [$f = 0$ for plot (b); $\epsilon = 0$ for all plots].

more structured as N increases, which reflects enhanced frequency selectivity.

At very high frequencies ($\omega\tau \gtrsim 10^7$), the curves converge to a baseline around 10^{-21}–10^{-23}, suggesting that additional pulses beyond a certain point offer diminishing returns in this regime. Overall, the filter functions show that higher-order CPMG sequences provide broader and deeper suppression of low-frequency noise, with tunable filtering properties governed by the pulse number.

The plots in Fig. 3(c) compare the filter functions F_{ij}/ω^2 for sequences $\mathcal{A}_1$ as the parameter f varies from 0 to 0.8. In the low-frequency regime ($\omega\tau \ll 1$) for $\mathcal{A}_1$, the function shifts from 4×10^{-9} ($f=0$) to 1.8×10^{-8} ($f=0.3$), suggesting an increment by ~ 4.5 times, while the peak amplitude remains stable (within 0.1%) at approximately 6.5×10^{-6} across values of $f \in (0, 0.3)$. In contrast, $\mathcal{B}_1$ at low frequencies shows a change in the function from 3×10^{-9} ($f=0$) to 4.5×10^{-7} ($f=0.3$), which is an increment by ~ 150 times. Further, the peak amplitude reduces by 3% (for $f=0$ to 0.3) and even undergoes a leftward shift and narrowing of the filter bandwidth.

These differences indicate that $\mathcal{B}_1$ is more sensitive to variations in f, with its filtering strength and spectral selectivity degrading significantly as f increases. In contrast, $\mathcal{A}_1$ maintains consistent filtering performance, making it ~ 30 times more robust under fluctuations in f (from 0 to 0.3). Thus, based on the stability of peak height, location, and shape, $\mathcal{A}_1$ is quantitatively more resilient to changes in f than $\mathcal{B}_1$. This approach is system agnostic, and shows robustness of sequence $\mathcal{A}$ over $\mathcal{B}$ irrespective of the dominant noise spectrum of hardware.

We now focus on SiV^--based system placed on the cold-plate stage (100 mK) of a dilution refrigerator. Implementing a pulse sequence ($\mathcal{A}$ or $\mathcal{B}$) leads to active and passive heat-loads on the sample stage, which depends on multiple parameters like: dilution fridge geometry and cooling cycle, thermal properties of cryogenic coax cable, sample footprint, specific heat capacity of the sample, and its thermal anchoring with the stage. Suppose for sequence $\mathcal{A}_N$, pulse incoming times are $t_{j,\mathcal{A}} = \{(2j-1)t_{\rm dds}/2N\}$, where $1 \le j \le N$, and for sequence $\mathcal{B}_N(m)$, the incoming times are $t_{jk,B} = \{(2j-1)t_{\rm dds}/2N + (k-1)t_{\pi,B}\}$, where $1 \le j \le N$ and $1 \le k \le m$. We assume a realistic set of device parameters and derive the following expressions for time-dependent temperature of SiV^- system $\Theta_{\rm SiV}$ [see Sec. III.F, Eq. (89) in the Supplemental Material [23]]:

$$\Theta_{\rm SiV}(t) = \overline{\Theta}_{\rm CP} + \sum_{j=1}^{N} \left(\Theta_{\rm SiV}(t,\, t_{j,\mathcal{A}}) - \overline{\Theta}_{\rm CP}\right) \quad \text{for } \mathcal{A}_N, \tag{16a}$$

$$\Theta_{\rm SiV}(t) = \overline{\Theta}_{\rm CP} + \sum_{j=1}^{N}\sum_{k=1}^{m} \left(\Theta_{\rm SiV}(t,\, t_{jk,B}) - \overline{\Theta}_{\rm CP}\right) \quad \text{for } \mathcal{B}_N(m). \tag{16b}$$

Here $\overline{\Theta}_{\rm CP}$ takes into account the slow temperature rise in the cold-plate as in Eq. (83) in the Supplemental Material [23], and $\Theta_{\rm SiV}(t, t_0)$ is given by

$$\Theta_{\rm SiV}(t, t_0) = \Theta_{\rm CP} + P_{\rm th}\left(e^{-\frac{t-t_0}{\tau_{\rm th,SiV}}} - e^{-9\frac{t-t_0}{\tau_{\rm th,SiV}}}\right) \times \mathrm{ReLU}(t-t_0), \tag{17}$$

where $P_{\rm th}$ is a normalization constant [estimated in Eq. (87) in the Supplemental Material [23]] and $\tau_{\rm th,SiV}$ is the thermalization timescale of the sample. Thus, while the dynamical decoupling pulses are applied, it simultaneously increases the temperature of the sample which impacts the T_2 and T_1 time of the system. Assuming that $1/T_{2(1)}$ of SiV^- has a linear dependence with $\Theta_{\rm SiV}$ in the low-temperature and low-strain regime [42,63], Eqs. (91) and (92) in the Supplemental Material [23] yield the following effective T_2 times for a measurement window $t_{\rm dds}$ in case of both sequences:

$$T_2(\Theta_{\rm SiV}(t_{\rm dds}, \mathcal{A}_N)) = \frac{T_2(0.1\,\mathrm{K}, \mathcal{A}_N)}{1 + T_2(0.1\,\mathrm{K}, \mathcal{A}_N)\cdot(\Theta_{\rm SiV}(t_{\rm dds}, \mathcal{A}_N) - 0.1)\cdot 3\cdot 10^6}, \tag{18a}$$

$$T_2(\Theta_{\rm SiV}(t_{\rm dds}, \mathcal{B}_N)) = \frac{T_2(0.1\,\mathrm{K}, \mathcal{B}_N)}{1 + T_2(0.1\,\mathrm{K}, \mathcal{B}_N)\cdot(\Theta_{\rm SiV}(t_{\rm dds}, \mathcal{B}_N) - 0.1)\cdot 3\cdot 10^6}. \tag{18b}$$

This implies that two competing effects are in play: (a) heat load due to the pulses decohering the system and (b) dynamical decoupling improving the coherence of the system. Figures 4(a)–4(c) show the rise of SiV^- temperature $\Theta_{\rm SiV}$ with CPMG index N, since the heat-load increases with N. For these simulations, we take $m = 121$ in $\mathcal{B}(m, \tau)$ to address the 121 qubits in the ϵ–f space. Further, as $t_{\rm dds}$ increases from 0.2 to 2 ms, the rise in $\Theta_{\rm SiV}$ reduces for both $\mathcal{A}$ and $\mathcal{B}$, due to the reduction of the duty cycle of the incoming pulses while $t_{\rm dds}$ increases. Since $\mathcal{B}$ leads

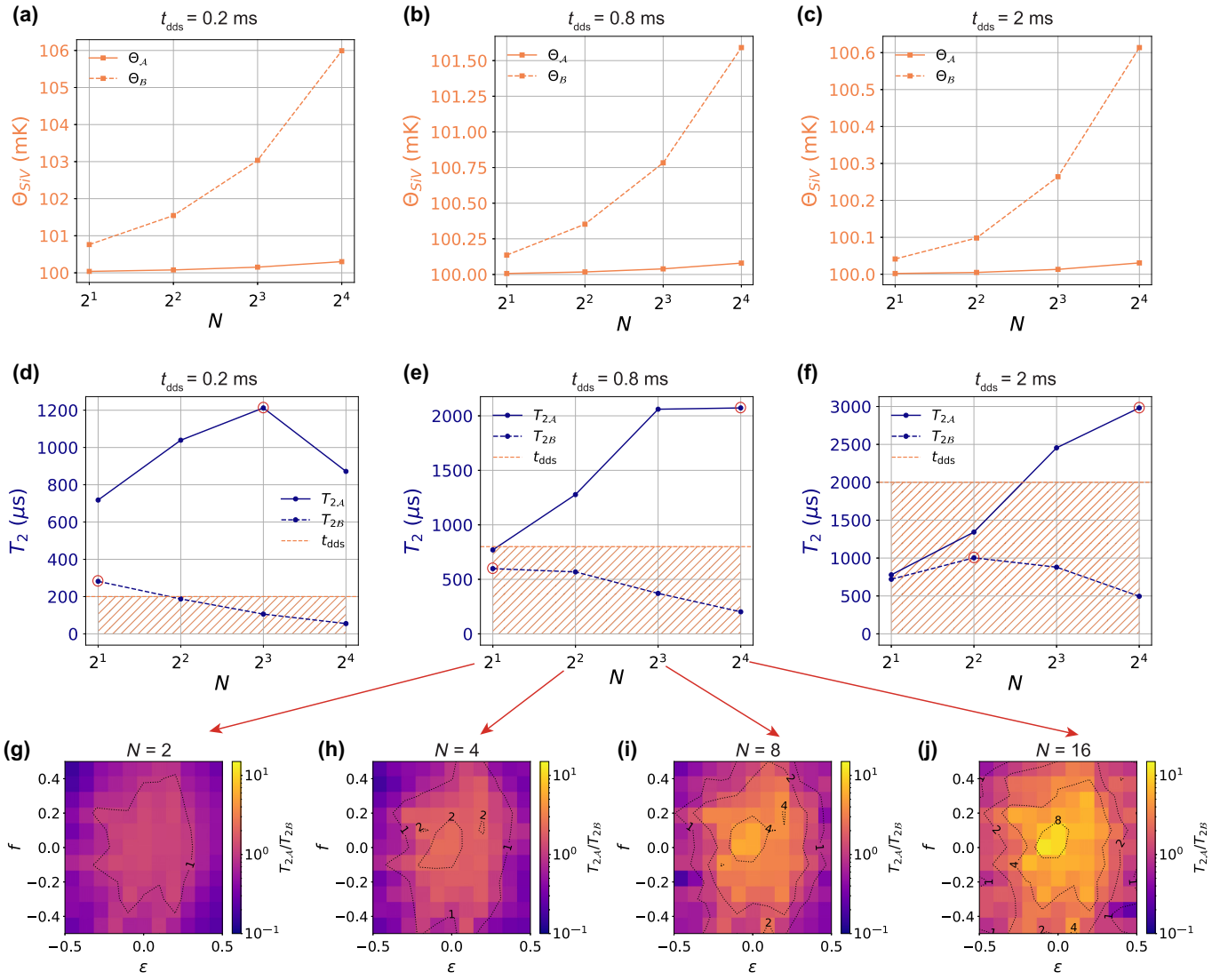


FIG. 4. Temperature and T_2 simulations. (a)–(c) Variation of SiV^- temperature Θ_{SiV} with the Carr-Purcell-Meiboom-Gill index N. Sequence $\mathcal{B}$ consistently leads to a higher rise in temperature compared to $\mathcal{A}$. As t_{dds} is increased, the rise in temperature reduces for both sequences due to the reduction in the duty cycle of the active heat load. (d)–(f) Variation of T_2 (for the central qubit, i.e. $\epsilon = f = 0$) with N. The orange shaded region represents the region $T_2 < t_{dds}$, signifying that the decoupling protocol is futile in that region. Red circles represent the optimal Carr-Purcell-Meiboom-Gill index (i.e. N for which T_2 is maximum), signifying the interplay between heat-induced decoherence and improved coherence due to dynamical decoupling. Furthermore, T_2 for sequence $\mathcal{A}$ is consistently larger than that for $\mathcal{B}$. As t_{dds} increases, T_2 values for both sequences increase but sequence $\mathcal{B}$ gets completely submerged in the shaded region [(e) and (f)]. This implies that decoupling via $\mathcal{B}$ does not work for larger values of t_{dds}. (g)–(j) For $t_{dds} = 0.8$ ms, we plot the heatmaps for $T_{2\mathcal{A}}/T_{2\mathcal{B}}$ on the composite (ϵ–f) search space. Here the dotted contours show islands where the ratio is above a marked threshold. As N increases, the contour landscape becomes more pronounced with maximum enhancement above 8 for $N = 16$. (m is set to 121 for $\mathcal{B}$ in the above simulations.).

to a larger heat-load into the sample compared to $\mathcal{A}$, we observe that for $t_{dds} = 0.2$ ms Θ_{SiV} increases by $\sim 5.2\%$ for $\mathcal{B}$ in contrast to a negligible rise of $\sim 0.3\%$ for $\mathcal{A}$. Since $\mathcal{B}$ consistently leads to larger SiV^- temperatures compared to $\mathcal{A}$, it leads to lower T_2 due to larger phonon-induced decoherence, as shown in Figs. 4(d)–4(f). Further, as t_{dds} increases from 0.2 to 2 ms, the T_2 value for both $\mathcal{A}$ and $\mathcal{B}$ increases, since the effective thermal load reduces with increase in t_{dds}. We also observe that for a particular value of t_{dds}, there exists an optimal value of N [encircled in red in Figs. 4(d)–4(f)] which maximizes T_2. The existence of this optimal value is a demonstration of the interplay between the two effects of heat-induced decoherence and increased coherence due to decoupling sequences. Tables I and II compare the coherence times $T_{2\mathcal{A}}$ and $T_{2\mathcal{B}}$ for two sequences across various pulse numbers N for two

TABLE I. Comparison of coherence times and mean enhancement for $t_{\mathrm{dds}} = 0.2\,\mathrm{ms}$. Values shown are (mean ± standard deviation) over the grid points.

N	$T_{2\mathcal{A}}$ (ms)	$T_{2\mathcal{B}}$ (ms)	Enhancement
2	$0.43^{\pm 0.18}$	0.28	1.5
4	$0.51^{\pm 0.27}$	0.19	2.7
8	$0.49^{\pm 0.29}$	0.10	4.7
16	$0.39^{\pm 0.19}$	0.06	7.2

different values of t_{dds}. The numbers reported here are the average and standard deviation over all grid points in the composite search space. Sequence $\mathcal{A}$ consistently produces longer coherence times than sequence $\mathcal{B}$, with enhancement factors extending to 7. Table II shows that for larger values of t_{dds} the enhancement ratio reduces because the heat-load due to $\mathcal{B}$ approaches the heat-load due to $\mathcal{A}$ as seen from Figs. 4(a)–4(c).

The orange shaded regions in Figs. 4(d)–4(f) represent the region for which $T_2 < t_{\mathrm{dds}}$, indicating that any pulse sequence within that region is not useful for dynamical decoupling. For lower values of $t_{\mathrm{dds}} = 0.2\,\mathrm{ms}$, $\mathcal{B}$ is within this region for $N > 2$ whereas $\mathcal{A}$ always stays outside. Increasing t_{dds} completely submerges $\mathcal{B}$ in this region, implying that $\mathcal{B}$ cannot be used for dynamical decoupling at all for larger values of t_{dds}. Sequence $\mathcal{A}$ is now only partially submerged, implying that $\mathcal{A}$ not just shows enhancement in T_2, but due to a lower heat-load it also performs useful dynamical decoupling. Figures 4(g)–4(j) show the 2D-color map of the enhancement ratio for $t_{\mathrm{dds}} = 0.8\,\mathrm{ms}$ and various N. The contours represent fixed enhancement ratios. As N increases, we observe larger contour landscapes with some enhancement values extending even beyond 8. The fact that our robust global pulse (sequence $\mathcal{A}$) outperforms even this idealized, best-case *steelman* version of sequence $\mathcal{B}$ is the critical result. It serves as a definitive proof of superiority: if sequence $\mathcal{A}$ wins against a "perfect" sequence $\mathcal{B}$, it will inherently dominate a "realistic" sequence $\mathcal{B}$, where crosstalk would degrade the baseline fidelity significantly further. Thus, our results represent a lower bound on the performance advantage of the SAFE-GRAPE approach.

This section shows that the dynamical decoupling sequence implemented by the SAFE-GRAPE optimized unitaries outperforms traditional bang-bang sequences in terms of: heat-load (Θ_{SiV} increases by $\sim 5.2\%$ for $\mathcal{B}$ and $\sim 0.3\%$ for $\mathcal{A}$), T_2 enhancement (reaching over 7), and feasibility ($\mathcal{B}$ stops to decouple noise for larger values of t_{dds}). In the Supplemental Material [23], we further change the number of qubits m from 10^2 to 10^4 and observe that as the number of qubits scale, protocol $\mathcal{B}$ goes completely within the orange shaded region, implying that approach $\mathcal{B}$ is non-scalable for dynamical decoupling. Hence we have created a phase-noise-reduced platform, which can be used to implement the single-photon entanglement protocol of the next section.

TABLE II. Comparison of coherence times and mean enhancement for $t_{\mathrm{dds}} = 0.8\,\mathrm{ms}$. Values shown are (mean ± standard deviation) over the grid points.

N	$T_{2\mathcal{A}}$ (ms)	$T_{2\mathcal{B}}$ (ms)	Enhancement
2	$0.45^{\pm 0.19}$	0.59	0.75
4	$0.58^{\pm 0.34}$	0.57	1.0
8	$0.65^{\pm 0.47}$	0.37	1.8
16	$0.62^{\pm 0.44}$	0.20	3.0

III. APPLICATION TO QUANTUM COMPUTATION

A. Entanglement operations and cluster-state generation

We implement a single-photon protocol [16] for entanglement generation and start from the following initial state:

$$\psi_{in}(\alpha,\phi) = \sqrt{\alpha}\,|0\rangle + \sqrt{1-\alpha}\,e^{i\phi}\,|1\rangle\,, \tag{19}$$

as seen in Fig. 1(b). The checkerboard configuration in ϵ–f space, from Fig. 5 is taken as an example where two qubits j (system A) and k (system B) are highlighted. We take a statistical approach to describe the resulting quantum volume. In order to generate a first successful entanglement link between qubits j and k, one has to wait for a sufficient number of attempts m_{jk}. m_{jk} is a random variable following a geometric distribution $P_{jk}(m) = 2\alpha\eta(1-2\alpha\eta)^{m-1}$, where η is the single-photon detection efficiency [see Sec. III, Eq. (32) in the Supplemental Material [23]]. For our simulations, we take $(\alpha,\eta) = (10^{-4}, 10^{-2})$. This means that the process of cluster-state generation creates a distribution $\mathcal{D}_m$ of waiting times, and a distribution $\mathcal{D}_{\mathcal{F}}$ of the fidelity for the entanglement link generated between each of the total N_q^2 pairs,

$$\begin{aligned}\mathcal{D}_m &= \{m_{jk}\}_{\substack{1\le i\le N_q\\ 1\le j\le N_q}},\\ \mathcal{D}_{\mathcal{F}} &= \{\mathcal{F}_{jk}\}_{\substack{1\le i\le N_q\\ 1\le j\le N_q}}.\end{aligned} \tag{20}$$

From Sec. II.C, we get for each qubit j a triplet $(\epsilon_j, z_j, T_{2j})$, which are the gate error, T_2 scaling and T_2 time. Section III.E in the Supplemental Material [23] yields the following expression for the lower bound on the ensemble-averaged entanglement fidelity for the pair jk as a function of the experimental time duration τ $(= t_{\mathrm{dds}} + t_{\mathrm{cmpl}})$ [23],

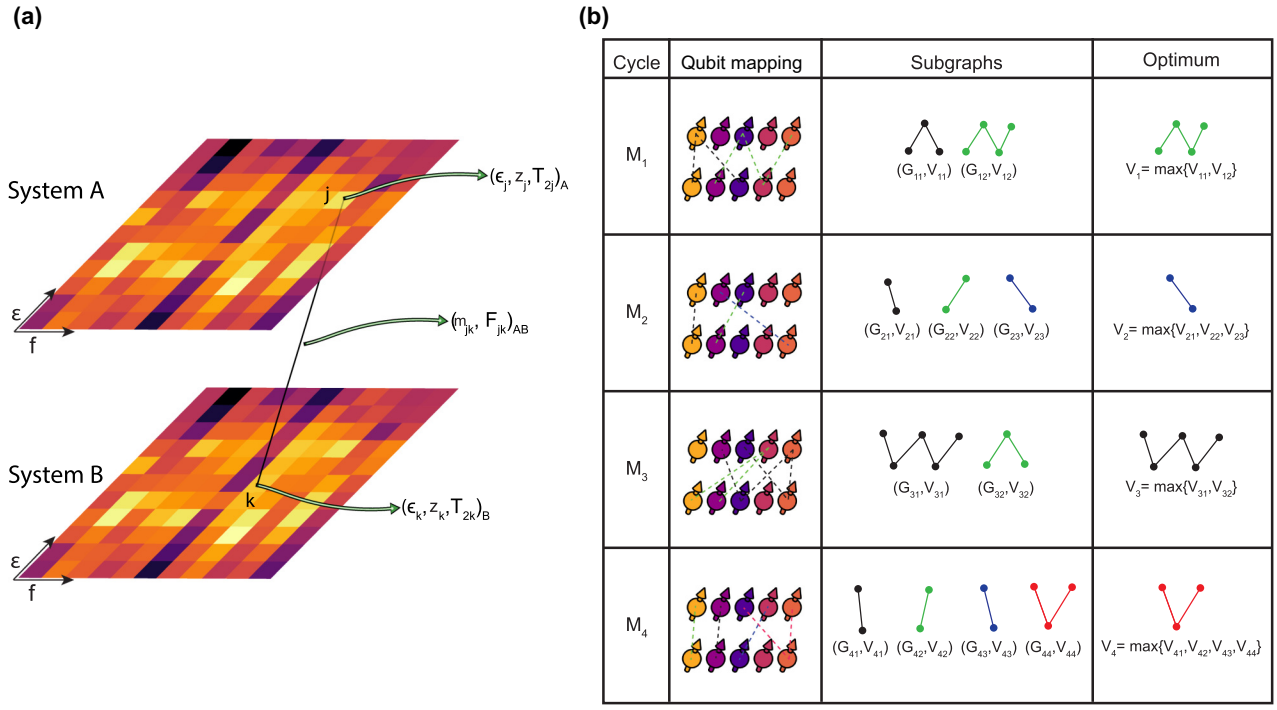


FIG. 5. Entanglement links statistics. (a) Checkerboard representation (ϵ–f space) of two systems, in which qubit j (system A) and k (system B) is highlighted (colors only represent inhomogeneity and have no physical significance); an entanglement attempt on j–k, leads to a success after waiting for m_{jk} attempts with a fidelity F_{jk}. (b) A graphical representation of the qubits over four different experimental cycles, where M_i shows the ith experimental cycle. For any experimental cycle, the policy produces different configurations of subgraphs G_{ij} with quantum volume V_{ij} corresponding to the j th cluster of the ith experimental cycle.

$$\overline{\mathcal{F}_{jk}(\alpha,\tau)} \geq \left(1 - e^{-\frac{\tau}{T_1}}\alpha - (1 - e^{-\frac{\tau}{T_1}})p_{\text{th}}(\tau)\right)\left(\frac{1 + e^{-((\tau/T_{2j})^{z_j} + (\tau/T_{2k})^{z_k})} - \sqrt{1 - e^{-2(\tau/T_{2j})^{z_j}}}\sqrt{1 - e^{-2(\tau/T_{2k})^{z_k}}}}{2}\right). \quad (21)$$

Here the overline represents an ensemble average over multiple measurement attempts leading to averaging over the noise bath, and p_{th} is the thermodynamic steady-state probabilities given by the following Boltzmann distribution:

$$p_{\text{th}} = \frac{1}{1 + e^{-\hbar\omega/(k_B\Theta_{\text{SiV}})}}, \quad (22)$$

where $\hbar\omega$ is the energy of the qubit and k_B is the Boltzmann constant. All three parameters: T_2, T_1, p_{th} depend on τ through the following mapping: $\{T_2, T_1, p_{\text{th}}\} \rightarrow \Theta_{\text{SiV}} \rightarrow \tau$. Each measurement cycle, leads to a bipartite graph $\mathcal{G}_\tau$ with edges given by the set $\mathcal{A}_\tau$. Suppose that $\mathcal{G}_\tau$ is a union of $\mathcal{K}_\tau$ disconnected subgraphs, then we have the following expressions:

$$\mathcal{G}_\tau = \{(j,k) \mid m_{jk} < M\},$$
$$\mathcal{G}_\tau = \bigoplus_{i=1}^{\mathcal{K}_\tau} \mathcal{G}_\tau^i, \quad (23)$$

where M is the total number of attempts [Fig. 1(b)] and $\mathcal{G}_\tau^i$ is the ith connected subgraph of $\mathcal{G}_\tau$. We represent the set of edges and nodes in $\mathcal{G}_\tau^i$ by $\mathcal{E}_\tau^i$, $\mathcal{N}_\tau^i$ respectively. Each subgraph $\mathcal{G}_\tau^i$ acts as a quantum computational substrate with its quantum volume defined as [53,64]

$$\log_2(\mathrm{V}_\tau^i) = \underset{2\leq n\leq|\mathcal{N}_\tau^i|}{\text{argmax}} \min\left(n, \frac{1}{n\epsilon_{\text{eff}}}\right) \leq \left\lfloor \frac{1}{\sqrt{\epsilon_{\text{eff}}}} \right\rfloor. \quad (24)$$

Here ϵ_{eff} is the average two-qubit gate error over all possible links (j-k) such that $\overline{\epsilon_{jk}} < 0.5$ given by

$$\epsilon_{\text{eff}} = \frac{1}{n_{\text{links}}(t_{\text{dds}}, t_{\text{cmpl}})} \times \sum_{\substack{(j,k)\in\mathcal{G}_\tau \\ \overline{\epsilon_{jk}}<0.5}} \overline{\epsilon_{jk}}(\alpha, t_{\text{dds}}, t_{\text{cmpl}}, N.) \quad (25)$$

Here, $n_{\text{links}}(t_{\text{dds}}, t_{\text{cmpl}})$ is the number of links such that $\overline{\epsilon_{jk}} < 0.5$, t_{dds} is the time window for decoupling sequences, t_{cmpl}

is the compilation time [Fig. 1(b)], N is the CPMG pulse index, and $\epsilon_{jk}(\alpha,\tau)$ is an ensemble-averaged two-qubit gate error on the link j-k over experimental duration τ. The expression for ϵ_{jk} and its temporal average $\overline{\epsilon_{jk}}$ is derived in Secs. III.E and III.F in the Supplemental Material [23]:

$$\epsilon_{jk}(\alpha,\tau,N) = 1 - \left(1 - e^{-\frac{\tau}{T_1}}\alpha - (1 - e^{-\frac{\tau}{T_1}})\, p_{\text{th}}\right) \times \left(\frac{1 + e^{-((\tau/T_{2j})^{z_j} + (\tau/T_{2k})^{z_k})} - \sqrt{1 - e^{-2(\tau/T_{2j})^{z_j}}}\sqrt{1 - e^{-2(\tau/T_{2k})^{z_k}}}}{2}\right) + (2N+1)\epsilon_{1\text{-qubit}}, \tag{26a}$$

$$\overline{\epsilon_{jk}}(\alpha, t_{\text{dds}}, t_{\text{cmpl}}, N) = \frac{1}{t_{\text{cmpl}}}\int_{t_{\text{dds}}}^{t_{\text{dds}}+t_{\text{cmpl}}} \epsilon_{jk}(\alpha,\tau,N)\, d\tau. \tag{26b}$$

The first term in Eq. (26a) is the error due to entanglement (which we approximate as CNOT gate error) and the second term is the local unitary (single-qubit) error. Equation (26a) follows from the universality theorem [65] stating that any two-qubit gate can be represented as a combination of a CNOT gate and single-qubit unitary. Since the entanglement process occurs stochastically in the time window $t = (t_{\text{dds}}, t_{\text{dds}} + t_{\text{cmpl}})$, we take the temporal average of $\epsilon_{jk}(\alpha,\tau,N)$ over this window. We can then estimate ϵ_{eff} by plugging Eqs. (26a) and (26b) in Eq. (25). We report two figures of merits for the cluster-state generation: $\epsilon_{\text{eff}}(t_{\text{dds}}, t_{\text{cmpl}}, N)$ and n_{links}.

We perform the entanglement error simulations over two systems (for $t_{\text{dds}} = \{0.2\,\text{ms}, 0.8\,\text{ms}\}$ and $t_{\text{cmpl}} = 10\,\mu\text{s}$), each containing 121 grid points (in ϵ–f space), implying that the total number of links are $121^2 (= 14\,641)$; here $m = 121$ is a modeling choice corresponding to a 11×11 discretization of the (ϵ, f) error space, which we interpret as 121 physically distinct, addressable emitters in a single device [43,66–68]. For low values of $t_{\text{dds}} = 0.2$ ms, we observe from Fig. 6(a) that n_{links} for $\mathcal{B}$ ($N = 2$) starts off high at 14 641 but sharply reduces to 0 for $N > 2$, which is supported by Fig. 4(d), where $\mathcal{B}$ is submerged in the shaded region for $N > 2$. In contrast, $\mathcal{A}$ varies from roughly 10 000 to 6000 with increase in N. Thus, for $t_{\text{dds}} = 0.2$ ms, n_{links} of $\mathcal{A}$ exceeds that of $\mathcal{B}$ by approximately $O(10^3$–$10^4)$. For $t_{\text{dds}} = 0.8$ ms n_{links} for $\mathcal{B}$ is zero for all N, whereas n_{links} achieves an optimal value at ∼900 for $\mathcal{A}_8$. This is shown in Figs. 6(a) and 6(b). Figures 6(c) and 6(d) show the variation of ϵ_{eff} with N, where the orange shaded area represents the region for which $\epsilon_{\text{eff}} > 0.5$. All sequences within this region give $n_{\text{links}} = 0$. For $t_{\text{dds}} = 0.2$ ms $\mathcal{B}$ starts off outside this region but enters it for $N > 2$, whereas $\mathcal{A}$ is consistently outside the shaded region up to $N = 16$. For $t_{\text{dds}} = 0.8$ ms, $\mathcal{B}$ is always inside the shaded region, whereas $\mathcal{A}$ starts from this region, but exits it for $N > 2$. Moreover it attains an optimal value for $N = 8$. The existence of an optimal N (encircled in red) is again a signature of two competing effects as discussed previously. Thus, for $t_{\text{dds}} = 0.8$ ms, n_{links} for $\mathcal{A}$ exceeds that of $\mathcal{B}$ by approximately $O(10^2$–$10^3)$. Tables III and IV summarize these values for the two sequences.

This section shows that the SAFE-GRAPE-based entanglement protocol outperforms conventional bang-bang CPMG in terms of: the number of entanglement links (exceeding by $O(10^2$–$10^4)$, depending on the temporal window of the dynamical decoupling sequences) and feasibility ($\mathcal{B}$ is unable to create links with $\overline{\epsilon_{jk}} < 0.5$ for larger values of t_{dds}).

B. Programmability and compilation

The task of programmability and compilation of color-center qubits relies on the assumption (see Sec. III C) that there exists a strain regime where there is a one-to-one mapping $\mathbb{F}_{aj}$ from the strain applied on system A, to the optical frequency of qubit j as follows:

$$\begin{aligned} f_j(t) &= \mathbb{F}_{aj}(s_a(t)), \\ f_j &= \mathbb{F}_{aj}(s_a), \end{aligned} \tag{27}$$

where $f_j(t)$ is the time-dependent optical transition frequency of qubit j, due to the slow modulation in the strain $s_a(t)$. Assuming that we are in the strain regime where $\mathbb{F}_{aj}$ is invertible, we have the following:

$$s_a = \mathbb{F}_{aj}^{-1}(f_j). \tag{28}$$

To define the strain which leads to the optical frequency equal to the laser frequency f_L, we adapt the following

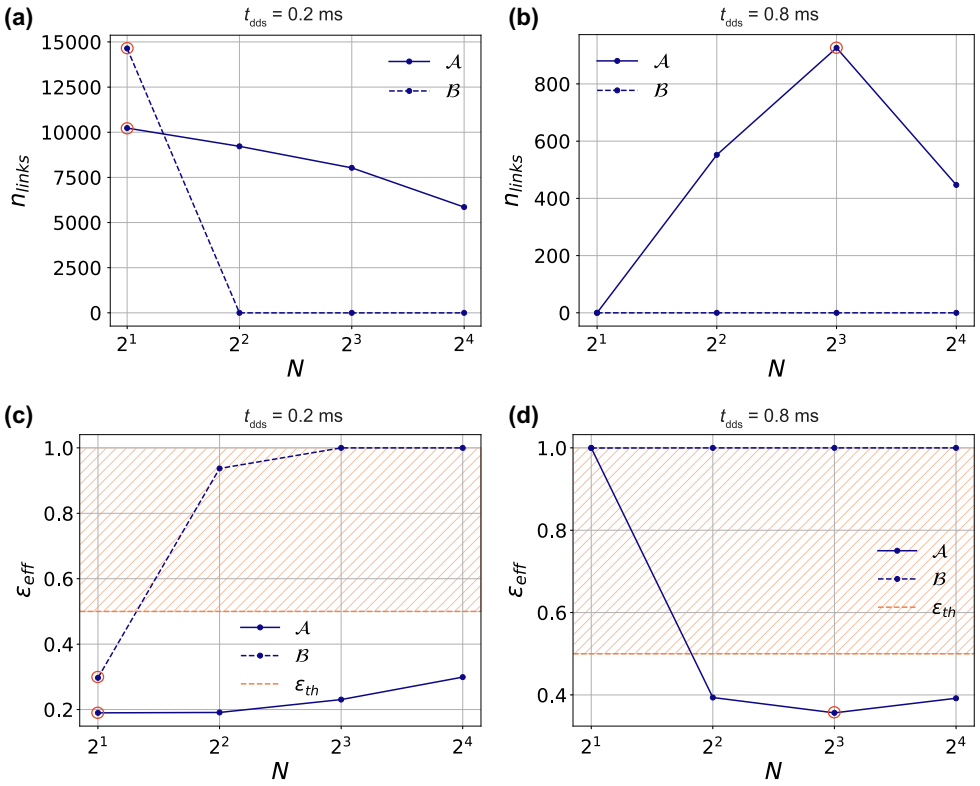


FIG. 6. Entanglement simulations. Simulations over two systems (each system containing 121 points on the ϵ–f space), with $121^2 (= 14\,641)$ possible links. Here n_{links} is the number of links which give effective error $\epsilon_{\text{eff}} < 0.5$ and the red circle represents the optimal value of N which maximizes n_{links} and minimizes ϵ_{eff}. For these simulations $t_{\text{cmpl}} = 10\,\mu\text{s}$. (a) For a low value of $t_{\text{dds}} = 0.2\,\text{ms}$, $\mathcal{B}$ starts off ($N = 2$) with performing better than $\mathcal{A}$, but for $N > 2$, n_{links} for $\mathcal{B}$ drops to zero as also confirmed from Fig. 4(d) where sequence $\mathcal{B}$ is completely submerged in shaded region for $N > 2$. On the contrary n_{links} for $\mathcal{A}$ is consistent around $\sim$ 5000–10 000. (b) For a larger value of $t_{\text{dds}} = 0.8\,\text{ms}$, n_{links} for $\mathcal{B}$ drops to zero for all N which is confirmed from Fig. 4(e) where $\mathcal{B}$ is completely submerged in the shaded region, whereas $\mathcal{A}$ reaches an optimum value of $\sim$ 900 for $N = 8$, and thus performs better than $\mathcal{B}$. (c) and (d) Variation of ϵ_{eff} with N (with the orange region showing the region $\epsilon_{\text{eff}} > 0.5$). For $t_{\text{dds}} = 0.2\,\text{ms}$, $\mathcal{B}$ gets submerged in the orange region for $N > 2$ whereas $\mathcal{A}$ is consistently outside the shaded region, always having a lower ϵ_{eff} than $\mathcal{B}$. For $t_{\text{dds}} = 0.8\,\text{ms}$, $\mathcal{B}$ is always submerged in the shaded region. $\mathcal{A}$ starts off from the shaded region, but already for $N > 2$ it exits it, achieving an optimal value for $N = 8$. For large t_{dds}, $\mathcal{A}$ consistently outperforms $\mathcal{B}$.

definition [Fig. 7(a.i)]:

$$s_{aj} = \mathbb{F}_{aj}^{-1}(f_L), \tag{29}$$

which leads to a set of strains $\{s_{aj}\}_{1 \le j \le N_a}$, where $N_{a(b)}$ is the number of qubits in system A(B). Without loss of generality, we can assume that the qubits are labeled such that the sequence is strictly monotonic,

$$s_{a1} < s_{a2} < \cdots < s_{aj} < \cdots < s_{aN_a}. \tag{30}$$

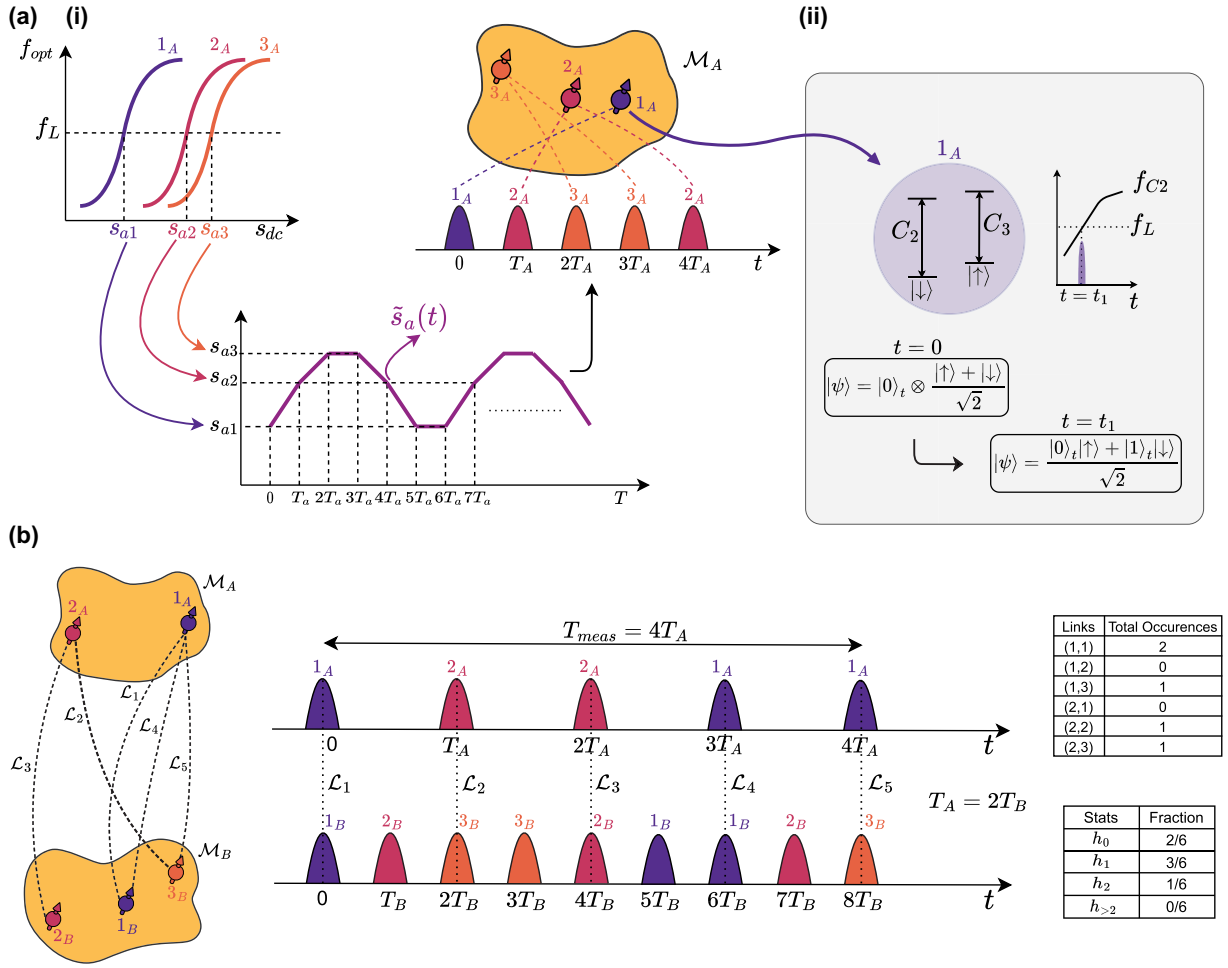
Figure 7(a.ii) shows the schematic for a laser interacting with a 4-level system to generate spin-photon entanglement, where the photonic qubit is encoded in the time-bin basis. The task of generating spin-photon entanglement at timestamps: $\{0, T_a, 2T_a, \ldots, (N_a - 1)T_a\}$ can be solved by

TABLE III. Comparison of entanglement link statistics for $t_{\text{dds}} = 0.2\,\text{ms}$ and $t_{\text{cmpl}} = 10\,\mu\text{s}$.

N	$n_{\text{links},\mathcal{A}}$	$n_{\text{links},\mathcal{B}}$	$\epsilon_{\text{eff},\mathcal{A}}$	$\epsilon_{\text{eff},\mathcal{B}}$
2	10 231	14 641	0.19	0.29
4	9221	0	0.19	0.94
8	8029	0	0.23	1.0
16	5857	0	0.30	1.0

TABLE IV. Comparison of entanglement link statistics for $t_{\text{dds}} = 0.8\,\text{ms}$ and $t_{\text{cmpl}} = 10\,\mu\text{s}$.

N	$n_{\text{links},\mathcal{A}}$	$n_{\text{links},\mathcal{B}}$	$\epsilon_{\text{eff},\mathcal{A}}$	$\epsilon_{\text{eff},\mathcal{B}}$
2	0	0	1.0	0.999
4	552	0	0.39	0.9999
8	926	0	0.36	1.0
16	447	0	0.39	1.0



Links	Total Occurences
(1,1)	2
(1,2)	0
(1,3)	1
(2,1)	0
(2,2)	1
(2,3)	1

Stats	Fraction
h_0	2/6
h_1	3/6
h_2	1/6
$h_{>2}$	0/6

FIG. 7. Programmability and entanglement compilation. (a.i) Schematic for Algorithm 1 illustrated for three qubits (in purple, crimson, and orange colors), where one first starts with the curve f_{opt} (optical frequency) vs s_{dc} (DC-strain), then maps it onto the time plot to construct the global strain drive $\tilde{s}_a(t)$, which leads to a train of spin-photon entanglements (photonic time-bin qubits are represented as colored pulses where the color matches that of the qubit with which it is entangled. (a.ii) Spin-photon entanglement generation per color-center at the timestep where laser frequency f_L matches its optical transition frequency. (b) Train of entangled time-bin qubits arriving at the beam-splitter from two systems in case of $T_A = 2T_B$. Every temporal coincidence between two pulse trains means an entanglement attempt between the respective remote qubits (Bell-state projection). For example at $t = T_A = 2T_B$, photonic qubit at T_A (entangled with qubit 2_A) temporally overlaps with photonic qubit at $2T_B$ (entangled with qubit 3_B). Hence, this is an entanglement attempt between qubits 2_A and 3_B (represented in dotted line by link $\mathcal{L}_2$). For a measurement window of $4T_A$ 4 unique links are attempted, leaving behind two links for all-to-all connectivity. The table on the right shows the link statistics and the number h_j represents the fraction of total possible links that occur j-times in a given window.

finding a global drive $\tilde{s}_a(t)$ for system A which satisfies the following condition:

$$\tilde{s}_a((k-1)\cdot T_a) = s_{ak} \qquad \forall k \in \{1, N_a\} \tag{31}$$

under the following constraints:

$$\begin{aligned} &(i) \quad T_a > 1/\gamma_{\text{opt}}, \\ &(ii) \quad \frac{d\tilde{s}_a(t)}{dt} < s_{\max}. \end{aligned} \tag{32}$$

The first constraint penalizes overlap between the emitted photons from different qubits, while the second constraint avoids sidebands due to strain modulation. We propose a simplistic solution based on Algorithm 1.

We use the same algorithm to compute the global drive for system B, $\tilde{s}_b(t)$ corresponding to a mapping sequence: $\{\mathbb{F}_{bj}\}_{1\le j\le N_b}$ and time sequence $\{kT_b\}_{0\le k\le (N_b-1)}$. Because of the way our global drive is constructed, spin-photon entanglement is established at the following time sequences $\mathcal{T}_{A(B)} \equiv \{kT_{a(b)}\}_{k\in\mathbb{W}}$. Further, the spin-photon entanglement at timestep $\mathcal{T}_{A(B)}(j)$ is with the spin-qubit labeled $\theta_{ja(b)}$, where qubit sequence $\mathcal{Q}_{A(B)} \equiv \{\theta_{ja(b)}\}$ is also termed

ALGORITHM 1. Computation of $\tilde{s}_a(t)$.

1: **Given sequences:** $\{\mathbb{F}_{aj}\}_{1\le j\le N_a}, \{kT_a\}_{0\le k\le (N_a-1)}$
2: **Evaluate:** $s_{aj} \leftarrow \mathbb{F}_{aj}^{-1}(f_L)$
3: **Assume (w.l.o.g.):** The sequence $\{s_{aj}\}$ is strictly monotonic.
4: $\beta_j \leftarrow \dfrac{s_{a,j+1} - s_{a,j}}{T_a}$
5: $\beta^* \leftarrow \max\{\beta_j\}$
6: $\kappa \leftarrow \dfrac{\beta^*}{s_{\max}}$
7: $T_a \leftarrow T_a(\mathrm{ReLU}(\kappa - 1) + 1)$
8: **for** $1 \le j \le N_a - 1$ **do**
9: **if** $(j-1)T_a \le t \le jT_a$ **then**
10: $\tilde{s}_a(t) \leftarrow \dfrac{s_{a,j+1} - s_{a,j}}{T_a}\, t + \Big(j\, s_{a,j} + (1-j)\, s_{a,j+1}\Big)$ ▷ Linear interpolation
11: **end if**
12: **end for**
13: **for** $N_aT_a \le t \le (2N_a - 1)T_a$ **do**
14: $\tilde{s}_a(t) \leftarrow \tilde{s}_a((2N_a - 1)T_a - t)$ ▷ Palindromic extension of $\tilde{s}_a(t)$
15: **end for**
16: **for** $t \ge 2N_aT_a$ **do**
17: $q \leftarrow \left\lfloor \frac{t}{2N_aT_a} \right\rfloor$
18: $\tilde{s}_a(t) \leftarrow \tilde{s}_a(t - 2N_aT_aq)$ ▷ Periodic extension of $\tilde{s}_a(t)$
19: **end for**
20: **return** $\tilde{s}_a(t)$

as a triangular-wave sequence which has the following compact form:

$$\theta_{ja(b)} = 1 + \min\Big\{j \bmod (2N_{a(b)}),\ (2N_{a(b)} - 1) - \big(j \bmod (2N_{a(b)})\big)\Big\}, \tag{33}$$

where j is in the set of whole numbers.

The second stage of compilation builds on the two time sequences $\mathcal{T}_A$ and $\mathcal{T}_B$. This stage is for creating entanglement link attempts efficiently between systems A and B, by overlapping the two timing sequences. We propose Algorithm 2 for this stage. Depending on the global strain drive, we can get different qubit mapping sequences $\mathcal{Q}_{A(B)}$. Because of the construction of Algorithm 1 (pseudocode: lines 14 and 18), where the global drive is forced to be palindromic and periodic in nature, the qubit sequence it creates has a triangular waveform structure as described in Eq. (33). This can be seen pictorially in Fig. 7(b). Algorithm 2 takes as an input these two-qubit mapping sequences $\{\mathcal{Q}_A, \mathcal{Q}_B\}$, and periodic timing sequences $\{\mathcal{T}_A, \mathcal{T}_B\}$. It finds the scaling m_{scal} $(= T_A/T_B)$, for which the number of unique entanglement links is maximized. This is demonstrated with an example in Fig. 7(b). We define the metric h_j as fraction of total possible links that occur j times in a given window. We see that for $T_{\mathrm{meas}} = 4T_A = 8T_B$, system A generates time-bin qubits $\{1_A, 2_A, 2_A, 1_A, 1_A\}$, whereas system B generates $\{1_B, 2_B, 3_B, 3_B, 2_B, 1_B, 1_B, 2_B, 3_B\}$. We see that temporal overlaps only lead to five entanglement attempts: $\{1_A - 1_B, 2_A - 3_B, 2_A - 2_B, 1_A - 1_B, 1_A - 3_B\}$.

Out of these five attempts we get the following statistics:

(1) links that occur exactly once: $\{2_A - 3_B, 2_A - 2_B, 1_A - 3_B\} \to h_1 = 3/6$,
(2) links that occur exactly twice: $\{1_A - 1_B\} \to h_2 = 1/6$,
(3) links that never occur: $\{1_A - 2_B, 2_A - 1_B\} \to h_0 = 2/6$.

These links statistics are also summarized in Fig. 7(b). Because of the construction of Algorithms 1 and 2, the fraction of attempted links $\sum_{i\ge 1} h_i$ satisfies the following inequality:

$$\sum_{i\ge 1} h_i \ge \frac{\max\{N_a, N_b\}}{N_aN_b}. \tag{34}$$

The above relation implies that using the combination of Algorithms 1 and 2, the number of unique entanglement links is bounded by order $\Omega(N_q)$. One can further improve this bound by sweeping on the value of m_{scal}.

ALGORITHM 2. Entanglement compiler.

Given: $\mathcal{Q}_A, \mathcal{Q}_B, T_a, T_b, N_a, N_b$
$E_{max} \leftarrow N_a N_b$
Assume: $T_a = T_b = T_0$
for $1 \leq m_{scal} \leq \min(N_a, N_b)$ **do**
  $T_a \leftarrow m_{scal} T_0$
  $j_{\max} \leftarrow \mathcal{J}(N_a, N_b, m_{scal})$ ▷ For derivation of $\mathcal{J}$, see Supplements
  for $0 \leq j \leq (j_{\max})$ **do**
    attempt entanglement link between qubits $\mathcal{Q}_A(j)$ and $\mathcal{Q}_B(m_{scal} j)$.
  end for
  $E(m_{scal}, N_a, N_b) \leftarrow$ total number of unique links made between $\mathcal{Q}_A$ and $\mathcal{Q}_B$
end for
$m^*_{scal} \leftarrow \min\{\text{argmin}_{m_{scal}} E(m_{scal}, N_a, N_b)\}$
$E^* \leftarrow E(m^*_{scal}, N_a, N_b)$
return m^*_{scal}, E^*

In Fig. 8 we show a more thorough analysis of our compilation algorithm. For all combinations of (N_a, N_b) qubits in the respective systems (illustrated for $N_b \leq N_a \leq 10$) we compute the optimal m_{scal} that minimizes the fraction of missing links h_0 [Figs. 8(a) and 8(b)]. Figure 8(c) shows the minimum required measurement window to achieve

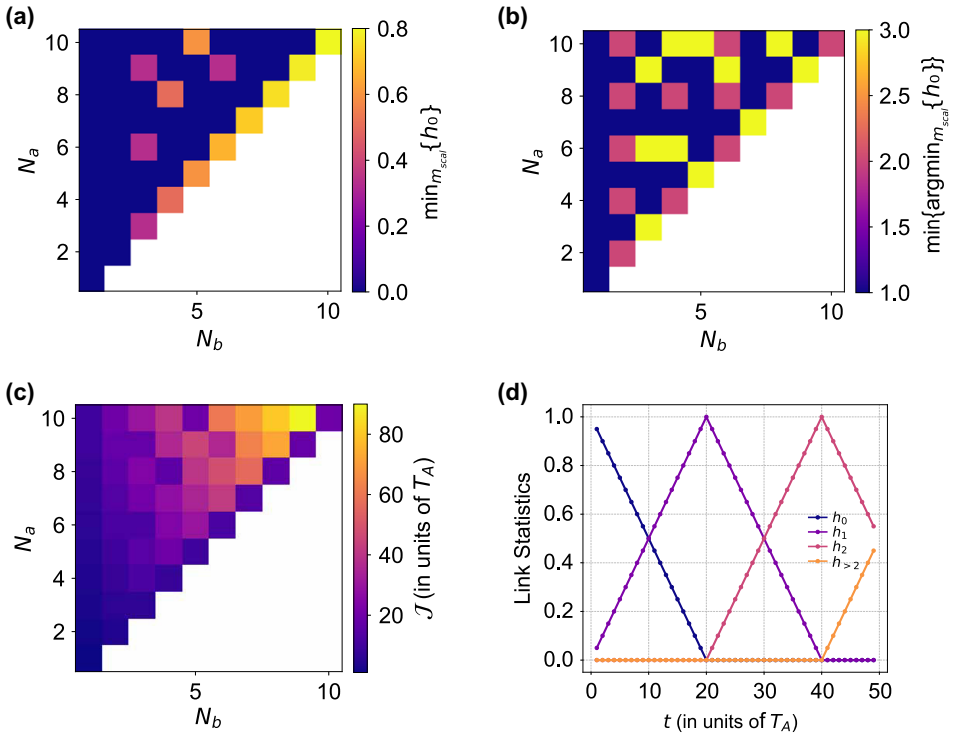


FIG. 8. Simulation for entanglement compilation (Algorithm 2). Here the number h_j represents the fraction of total possible links that occur j-times in an indefinite time window, and m_{scal} refers to the scaling between T_A and T_B (i.e. $T_A = m_{\text{scal}} T_B$). (a) Color map over the number of qubits in the two systems (N_a vs N_b), where the color quantifies the minimum h_0 (i.e. the fraction of links which never get entangled) obtained over any integer scaling m_{scal}. Dominant blue squares suggest there are multiple configurations $(N_a, N_b, m_{\text{scal}})$ for which $h_0 = 0$, implying all-to-all connectivity. (b) The scaling m_{scal} which minimizes h_0. (c) the minimum measurement window $t = \mathcal{J} T_A$, which minimizes h_0. (d) The trend for link statistics h_j as the measurement window t increases for the configuration $(N_a, N_b, m_{\text{scal}}) = (5, 4, 1)$.

the minimal h_0 in each of these scenarios. In Fig. 8(d) we show for a specific configuration how the link statistics evolve over time. In this specific case, we find that after time $t = 20T_A$ all possible links between qubits of both systems have been attempted.

C. Working strain window for Algorithm 1

Algorithm 1 requires a control parameter that drives every optical qubit *monotonically* and *injectively* past a global laser frequency f_L. We demonstrate that such a window exists on a state-of-the-art solid-state platform [43] by simulating the spin-conserving C_2 transition of several SiV^- centers in a nanomechanical structure, although the argument applies to any emitter whose lowest-order response to strain is linear.

For center i we decompose the strain that couples to the diamond E_{gx} mode into three additive terms

$$\epsilon_{E_{gx},i}(t) = \underbrace{\epsilon^{\text{bias}}_{E_{gx},i}}_{\text{fabrication}} + \underbrace{\epsilon^{\text{dc}}_{E_{gx}}}_{\text{piezo set–point}} + \underbrace{\epsilon^{\text{ac}}_{E_{gx}}(t)}_{\text{fast control}}, \tag{35}$$

so that in the low-strain limit ($|\epsilon_{E_{gx}}| \lesssim 10^{-4}$) the optical frequency is

$$f_{\text{opt},i} = f_0 + \Delta\, d\epsilon_{E_{gx},i}, \tag{36}$$

with

$$\Delta d = d_{es} - d_{gs} \simeq 0.5\,\text{PHz/strain}. \tag{37}$$

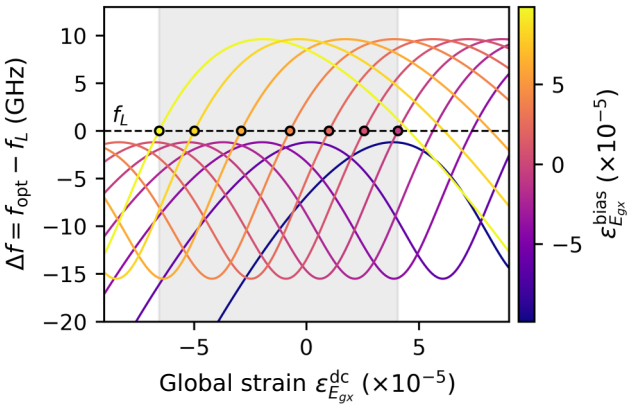


FIG. 9. Common monotonic strain window. Calculated detuning $\Delta f = f_{\text{opt}} - f_L$ for 11 SiV^- centers whose bias strains (color bar) span the $\sigma_\epsilon = 6 \times 10^{-5}$ distribution of Ref. [43], and arbitrary laser frequency. Black circles mark laser crossings detected within $|\Delta f| < 0.2$ GHz (C_2 transition linewidth) and with positive local slope. The shaded region extends from the earliest to the latest of these crossings and is truncated at the first additional (negative-slope) intersection of the outer-bias center, guaranteeing that the mapping $f_{\text{opt},i} = \mathbb{F}_{ai}(\epsilon^{\text{dc}}_{E_{gx}})$ is one-to-one for all qubits inside the band.

The static biases $\epsilon^{\text{bias}}_{E_{gx},i}$ are drawn from the Gaussian distribution $\mathcal{N}(0, \sigma_\epsilon)$ with $\sigma_\epsilon = 6 \times 10^{-5}$, derived from reported inhomogeneous C-transition spread in nanofabricated structures [43,69]. For simplicity, we assume only transverse-oriented SiV centers with $\epsilon_{yy} \neq 0, \epsilon_{xx} = \epsilon_{xz} = 0$, simulated by diagonalizing the full spin-orbit-Zeeman Hamiltonian with parameters detailed in Table S1 in the Supplemental Material [23].

Figure 9 shows the detuning $\Delta f = f_{\text{opt}} - f_L$ versus the piezo set-point $\epsilon^{\text{dc}}_{E_{gx}}$. We identify a strain regime (gray band) where every center crosses f_L exactly once with a positive slope, in order to fulfill the assumptions of Algorithm 1 for the entire ensemble. If a larger spectral spacing between crossings is required, one may simply omit the most crowded emitters without affecting the existence of the monotonic window.

IV. CONCLUSION AND OUTLOOK

We introduce a hardware-agnostic control-and-compilation framework that turns fabrication-induced inhomogeneity into a programmable resource for scalable quantum information processing. A single, globally applied strain drive—optimized via SAFE-GRAPE on a composite-pulse basis—implements uniform high-fidelity single-qubit gates across heterogeneous SiV^- ensembles. This approach corrects for significant variations in Rabi frequencies and spectral detunings to yield single-qubit gate fidelities exceeding 99.99% for normalized (with respect to Rabi strength) errors up to 0.3. Simulation results demonstrate that SAFE-GRAPE-based CPMG sequence $\mathcal{A}$ consistently outperforms alternative bang-bang-based CPMG sequence $\mathcal{B}$ across multiple performance metrics and operating regimes. In the low-frequency regime, $\mathcal{A}$ exhibits stable filtering behavior under variations in a detuning parameter f, with a modest 4.5-fold increase in low-frequency response and <0.1% variation in peak amplitude, compared to a 150-fold increase and 3% amplitude degradation for $\mathcal{B}$. This makes $\mathcal{A} \sim 30$ times more robust to parameter fluctuations, independent of the underlying noise spectrum.

In the decoupling regime, SAFE-GRAPE achieves a higher thermal robustness, with the heat-load parameter Θ_{SiV} increasing by approximately 5.2% for protocol $\mathcal{B}$ and 0.3% for protocol $\mathcal{A}$, while also delivering a significant coherence-time improvement, with T_2 enhancements reaching more than a factor of seven. Furthermore, unlike the bang-bang protocol, which ceases to suppress noise for large values of t_{dds}, SAFE-GRAPE maintains its feasibility, thereby enabling a phase-noise-reduced operational platform suitable for implementing the single-photon entanglement protocol.

In the entanglement generation stage, the SAFE-GRAPE-based protocol outperforms the bang-bang CPMG approach by achieving a markedly higher number of

successful entanglement links, exceeding by $O(10^2$–$10^4)$ depending on the temporal window of the decoupling sequences. This advantage is further reinforced by improved operational feasibility, as protocol $\mathcal{B}$ in the bang-bang case fails to generate high-fidelity links at large t_{dds}, whereas SAFE-GRAPE continues to operate effectively.

Finally, the theoretical analysis indicates that by employing the combination of Algorithms 1 and 2, the number of unique entanglement links generated by the system is guaranteed to be bounded by order $\Omega(N_q)$. This bound is not fundamental and can be improved further by sweeping over the scaling parameter m_{scal}, offering a path towards even greater scalability. Collectively, these results establish SAFE-GRAPE as a robust and scalable control strategy for both noise suppression and high-rate entanglement generation, paving the way for its integration into large-scale quantum networking architectures. We also provide an end-to-end framework, summarized as an effective quantum circuit diagram in Fig. 1(b), that delivers global control, dynamical decoupling, remote entanglement, and efficient compilation to build a bipartite cluster state.

Looking forward, the SAFE-GRAPE-optimized control pulses can be further improved by incorporating more advanced machine-learning-driven, *in situ* optimization techniques to adapt to dynamic changes in the qubit environment. On the hardware front, the performance can be enhanced by engineering nanomechanical structures with optimized mode shapes [70], enabling more efficient strain transfer and access to higher-frequency control regimes, although practical hurdles like charge-state instability will require parallel mitigation strategies.

The general nature of our framework ensures its applicability extends beyond the SiV^- center in diamond. It can be readily adapted to other promising strain-sensitive platforms, such as other group-IV color centers in diamond (SnV^- [5–7], GeV^- [71]) or defect centers in silicon [72–77] or silicon carbide (silicon vacancy V_{Si} [78]), thereby providing a general method for harnessing inhomogeneity in various solid-state systems.

Furthermore, the demonstrated global dynamical decoupling sequences can be repurposed for quantum sensing [79,80] and single-photon detection applications [81] (see Sec. V in the Supplemental Material [23]). Protecting the entire ensemble from decoherence simultaneously enhances its collective sensitivity to external fields, turning it into a parallelized quantum sensor. Further by utilizing the nuclear spin as memory qubits [45], the coherence timescale can be increased which allows us to perform more entanglement experiments in a given time. This boosts the entanglement success rate further.

Ultimately, this work lays the technical groundwork for measurement-based quantum processors built upon programmable quantum matter. By treating heterogeneity as a resource, our approach provides a practical roadmap towards networked demonstrations of multi-thousand-qubit cluster states, a critical step on the path to fault-tolerant quantum information systems.

CODE AVAILABILITY

The simulations were performed using `QuTiP` [82–84] and `PyTorch` [57] in Python. The codes can be found in our GitHub repository [85].

ACKNOWLEDGMENTS

The authors thank Dr. Matthew Trusheim, Dr. Hanfeng Wang, and Dr. Mahmoud Jalali Mehrabad for proofreading the manuscript and offering constructive feedback. We also thank Hamza Raniwala and Dr. Ian Christen for contributing to the initial discussions of this project. We thank Dr. Ethan G. Arnault for helpful discussions regarding the thermal modeling. P.A. would like to thank Amit and Deepali Sinha Foundation Presidential Fellowship from MIT, MITRE Quantum Moonshot Program, and NVIDIA Academic Grant Program. L.F. acknowledges support from the Air Force Office of Scientific Research (AFOSR) under Award No. GR108261. O.H. acknowledges support from the National Science Foundation (NSF) Engineering Research Center for Quantum Networks (CQN) awarded under cooperative agreement number 1941583.

D.R.E., P.A., L.F., and O.H. conceived the project. P.A. performed the simulations and theoretical work for filter functions, thermal model, entanglement fidelity, and compilation algorithms. L.F. performed simulations in strain modeling, thermal modeling, and entanglement protocol and contributed to the theory for the global unitary control and compilation algorithm. O.H. defined and implemented the SAFE-GRAPE algorithm for global unitary control and performed simulations for strain driving of SiV^- centers. P.A., L.F., and O.H. prepared the manuscript. All authors discussed the results and revised the manuscript. D.R.E. supervised the project.

The authors declare no competing interests.

DATA AVAILABILITY

The data that support the findings of this article are openly available [85].

[1] H. K. C. Beukers, M. Pasini, H. Choi, D. Englund, R. Hanson, and J. Borregaard, Remote-entanglement protocols for stationary qubits with photonic interfaces, PRX Quantum **5**, 010202 (2024).

[2] D. D. Sukachev, A. Sipahigil, C. T. Nguyen, M. K. Bhaskar, R. E. Evans, F. Jelezko, and M. D. Lukin, Silicon-vacancy spin qubit in diamond: A quantum memory exceeding

10 ms with single-shot state readout, Phys. Rev. Lett. **119**, 223602 (2017).

[3] J. Arjona Martínez, R. A. Parker, K. C. Chen, C. M. Purser, L. Li, C. P. Michaels, A. M. Stramma, R. Debroux, I. B. Harris, M. Hayhurst Appel *et al*., Photonic indistinguishability of the tin-vacancy center in nanostructured diamond, Phys. Rev. Lett. **129**, 173603 (2022).

[4] C. M. Knaut, A. Suleymanzade, Y.-C. Wei, D. R. Assumpcao, P.-J. Stas, Y. Q. Huan, B. Machielse, E. N. Knall, M. Sutula, G. Baranes *et al*., Entanglement of nanophotonic quantum memory nodes in a telecom network, Nature **629**, 573 (2024).

[5] T. Iwasaki, Y. Miyamoto, T. Taniguchi, P. Siyushev, M. H. Metsch, F. Jelezko, and M. Hatano, Tin-vacancy quantum emitters in diamond, Phys. Rev. Lett. **119**, 253601 (2017).

[6] R. A. Parker, J. Arjona Martínez, K. C. Chen, A. M. Stramma, I. B. Harris, C. P. Michaels, M. E. Trusheim, M. Hayhurst Appel, C. M. Purser, W. G. Roth *et al*., A diamond nanophotonic interface with an optically accessible deterministic electronuclear spin register, Nat. Photonics **18**, 156 (2024).

[7] A. E. Rugar, S. Aghaeimeibodi, D. Riedel, C. Dory, H. Lu, P. J. McQuade, Z.-X. Shen, N. A. Melosh, and J. Vučković, Quantum photonic interface for tin-vacancy centers in diamond, Phys. Rev. X **11**, 031021 (2021).

[8] S. D. Barrett and P. Kok, Efficient high-fidelity quantum computation using matter qubits and linear optics, Phys. Rev. A: At. Mol. Opt. Phys. **71**, 060310(R) (2005).

[9] H. Bernien, B. Hensen, W. Pfaff, G. Koolstra, M. S. Blok, L. Robledo, T. H. Taminiau, M. Markham, D. J. Twitchen, L. Childress *et al*., Heralded entanglement between solid-state qubits separated by three metres, Nature **497**, 86 (2013).

[10] B. Hensen, H. Bernien, A. E. Dréau, A. Reiserer, N. Kalb, M. S. Blok, J. Ruitenberg, R. F. Vermeulen, R. N. Schouten, C. Abellán *et al*., Loophole-free bell inequality violation using electron spins separated by 1.3 kilometres, Nature **526**, 682 (2015).

[11] P. C. Humphreys, N. Kalb, J. P. J. Morits, R. N. Schouten, R. F. L. Vermeulen, D. J. Twitchen, M. Markham, and R. Hanson, Deterministic delivery of remote entanglement on a quantum network, Nature **558**, 268 (2018).

[12] M. Pompili, S. L. N. Hermans, S. Baier, H. K. Beukers, P. C. Humphreys, R. N. Schouten, R. F. L. Vermeulen, M. J. Tiggelman, L. dos Santos Martins, B. Dirkse *et al*., Realization of a multinode quantum network of remote solid-state qubits, Science **372**, 259 (2021).

[13] P.-J. Stas, Y. Q. Huan, B. Machielse, E. N. Knall, A. Suleymanzade, B. Pingault, M. Sutula, S. W. Ding, C. M. Knaut, D. R. Assumpcao, Y.-C. Wei, M. K. Bhaskar, R. Riedinger, D. D. Sukachev, H. Park, M. Lončar, D. S. Levonian, and M. D. Lukin, Robust multi-qubit quantum network node with integrated error detection, Science **378**, 557 (2022).

[14] E. Bersin *et al.*, Telecom networking with a diamond quantum memory, PRX Quantum **5**, 010303 (2024).

[15] D. Dong and I. R. Petersen, Quantum control theory and applications: A survey, IET Control Theory Appl. **4**, 2651 (2010).

[16] S. L. N. Hermans, M. Pompili, L. D. Santos Martins, A. R-P Montblanch, H. K. C. Beukers, S. Baier, J. Borregaard, and R. Hanson, Entangling remote qubits using the single-photon protocol: An in-depth theoretical and experimental study, New J. Phys. **25**, 013011 (2023).

[17] M. Maronese, L. Moro, L. Rocutto, and E. Prati, Quantum compiling, in *Quantum Computing Environments* (Springer International Publishing, Cham, 2022), pp. 39–74.

[18] H. Wang, P. Liu, D. B. Tan, Y. Liu, J. Gu, D. Z. Pan, J. Cong, U. A. Acar, and S. Han, in *2024 ACM/IEEE 51st Annual International Symposium on Computer Architecture (ISCA)* (IEEE, Buenos Aires, Argentina, 2024), pp. 293–309.

[19] L. Li, P. Anand, K. He, and D. Englund, Dynamic inhomogeneous quantum resource scheduling with reinforcement learning, arXiv:2405.16380.

[20] A. Patil, M. Pant, D. Englund, D. Towsley, and S. Guha, Entanglement generation in a quantum network at distance-independent rate, npj Quantum Inf. **8**, 51 (2022).

[21] E. Kaur and S. Guha, Entanglement distribution in two-dimensional square grid network, arXiv:2306.03319.

[22] S. Krinner, S. Storz, P. Kurpiers, P. Magnard, J. Heinsoo, R. Keller, J. Luetolf, C. Eichler, and A. Wallraff, Engineering cryogenic setups for 100-qubit scale superconducting circuit systems, EPJ Quantum Technol. **6**, 2 (2019).

[23] See Supplemental Material at http://link.aps.org/supplemental/10.1103/kb8s-sffj for details on the driven-dissipative model, heralding protocol, numerical simulations, and additional analysis of cluster-state generation, which includes Refs. [2,16,22,25,43,49,51,52,54–56,59,63,65,86–89].

[24] L. Viola and S. Lloyd, Dynamical suppression of decoherence in two-state quantum systems, Phys. Rev. A **58**, 2733 (1998).

[25] C. T. Nguyen, D. D. Sukachev, M. K. Bhaskar, B. Machielse, D. S. Levonian, E. N. Knall, P. Stroganov, C. Chia, M. J. Burek, R. Riedinger *et al*., An integrated nanophotonic quantum register based on silicon-vacancy spins in diamond, Phys. Rev. B **100**, 165428 (2019).

[26] R. Jozsa, An introduction to measurement based quantum computation, NATO Science Series, III: Computer and Systems Sciences. Quantum Information Processing-From Theory to Experiment, (2006), 199, pp. 137–158.

[27] P. Kok, W. J. Munro, K. Nemoto, T. C. Ralph, J. P. Dowling, and G. J. Milburn, Linear optical quantum computing with photonic qubits, Rev. Mod. Phys. **79**, 135 (2007).

[28] M. Pompili, C. Delle Donne, I. te Raa, B. van der Vecht, M. Skrzypczyk, G. Ferreira, L. de Kluijver, A. J. Stolk, S. L. Hermans, P. Pawełczak *et al*., Experimental demonstration of entanglement delivery using a quantum network stack, npj Quantum Inf. **8**, 121 (2022).

[29] G. Ni, L. Ho, and H. Claussen, Entanglement request scheduling in quantum networks using deep q-network, in *ICC 2025-IEEE International Conference on Communications* (IEEE, 2025), pp. 4603–4608.

[30] E. Lucero, J. Kelly, R. C. Bialczak, M. Lenander, M. Mariantoni, M. Neeley, A. D. O'Connell, D. Sank, H. Wang, M. Weides, J. Wenner, T. Yamamoto, A. N. Cleland, and J. M. Martinis, Reduced phase error through optimized control of a superconducting qubit, Phys. Rev. A **82**, 042339 (2010).

[31] R. Jain, Z. Ji, S. Upadhyay, and J. Watrous, Qip = pspace, JACM, **58**, 1 (2011).

[32] M. A. Nielsen, Cluster-state quantum computation, Rep. Math. Phys. **57**, 147 (2006).
[33] C. Bradac, W. Gao, J. Forneris, M. E. Trusheim, and I. Aharonovich, Quantum nanophotonics with group IV defects in diamond, Nat. Commun. **10**, 5625 (2019).
[34] C. Hepp, T. Müller, V. Waselowski, J. N. Becker, B. Pingault, H. Sternschulte, D. Steinmüller-Nethl, A. Gali, J. R. Maze, M. Atatüre, and C. Becher, Electronic structure of the silicon vacancy color center in diamond, Phys. Rev. Lett. **112**, 036405 (2014).
[35] T. Iwasaki, F. Ishibashi, Y. Miyamoto, Y. Doi, S. Kobayashi, T. Miyazaki, K. Tahara, K. D. Jahnke, L. J. Rogers, B. Naydenov, F. Jelezko, S. Yamasaki, S. Nagamachi, T. Inubushi, N. Mizuochi, and M. Hatano, Germanium-vacancy single color centers in diamond, Sci. Rep. **5**, 12882 (2015).
[36] M. K. Bhaskar, D. D. Sukachev, A. Sipahigil, R. E. Evans, M. J. Burek, C. T. Nguyen, L. J. Rogers, P. Siyushev, M. H. Metsch, H. Park, F. Jelezko, M. Lončar, and M. D. Lukin, Quantum nonlinear optics with a germanium-vacancy color center in a nanoscale diamond waveguide, Phys. Rev. Lett. **118**, 223603 (2017).
[37] T. Iwasaki, Y. Miyamoto, T. Taniguchi, P. Siyushev, M. H. Metsch, F. Jelezko, and M. Hatano, Tin-vacancy quantum emitters in diamond, Phys. Rev. Lett. **119**, 253601 (2017).
[38] R. Debroux, C. P. Michaels, C. M. Purser, N. Wan, M. E. Trusheim, J. Arjona Martínez, R. A. Parker, A. M. Stramma, K. C. Chen, L. de Santis, E. M. Alexeev, A. C. Ferrari, D. Englund, D. A. Gangloff, and M. Atatüre, Quantum control of the tin-vacancy spin qubit in diamond, Phys. Rev. X **11**, 041041 (2021).
[39] H. K. C. Beukers, C. Waas, M. Pasini, H. B. van Ommen, Z. Ademi, M. Iuliano, N. Codreanu, J. M. Brevoord, T. Turan, T. H. Taminiau, and R. Hanson, Control of solid-state nuclear spin qubits using an electron spin-1/2, Phys. Rev. X **15**, 021011 (2025).
[40] C. D. Clark, H. Kanda, I. Kiflawi, and G. Sittas, Silicon defects in diamond, Phys. Rev. B **51**, 16681 (1995).
[41] J. P. Goss, R. Jones, S. J. Breuer, P. R. Briddon, and S. Öberg, The twelve-line 1.682 eV luminescence center in diamond and the vacancy-silicon complex, Phys. Rev. Lett. **77**, 3041 (1996).
[42] B. Pingault, D.-D. Jarausch, C. Hepp, L. Klintberg, J. N. Becker, M. Markham, C. Becher, and M. Atatüre, Coherent control of the silicon-vacancy spin in diamond, Nat. Commun. **8**, 15579 (2017).
[43] S. Meesala *et al.*, Strain engineering of the silicon-vacancy center in diamond, Phys. Rev. B **97**, 205444 (2018).
[44] M. H. Metsch, K. Senkalla, B. Tratzmiller, J. Scheuer, M. Kern, J. Achard, A. Tallaire, M. B. Plenio, P. Siyushev, and F. Jelezko, Initialization and readout of nuclear spins via a negatively charged silicon-vacancy center in diamond, Phys. Rev. Lett. **122**, 190503 (2019).
[45] M. K. Bhaskar, R. Riedinger, B. Machielse, D. S. Levonian, C. T. Nguyen, E. N. Knall, H. Park, D. Englund, M. Lončar, D. D. Sukachev, and M. D. Lukin, Experimental demonstration of memory-enhanced quantum communication, Nature **580**, 60 (2020).
[46] A. Sipahigil, K. D. Jahnke, L. J. Rogers, T. Teraji, J. Isoya, A. S. Zibrov, F. Jelezko, and M. D. Lukin, Indistinguishable photons from separated silicon-vacancy centers in diamond, Phys. Rev. Lett. **113**, 113602 (2014).
[47] E. N. Knall, C. M. Knaut, R. Bekenstein, D. R. Assumpcao, P. L. Stroganov, W. Gong, Y. Q. Huan, P.-J. Stas, B. Machielse, M. Chalupnik, D. S. Levonian, A. Suleymanzade, R. Riedinger, H. Park, M. Lončar, M. K. Bhaskar, and M. D. Lukin, Efficient source of shaped single photons based on an integrated diamond nanophotonic system, Phys. Rev. Lett. **129**, 053603 (2022).
[48] Y.-C. Wei, P.-J. Stas, A. Suleymanzade, G. Baranes, F. Machado, Y. Q. Huan, C. M. Knaut, S. W. Ding, M. Merz, E. N. Knall, U. Yazlar, M. Sirotin, I. W. Wang, B. Machielse, S. F. Yelin, J. Borregaard, H. Park, M. Lončar, and M. D. Lukin, Universal distributed blind quantum computing with solid-state qubits, Science **388**, 509 (2025).
[49] N. Khaneja, T. Reiss, C. Kehlet, T. Schulte-Herbrüggen, and S. J. Glaser, Optimal control of coupled spin dynamics: Design of NMR pulse sequences by gradient ascent algorithms, J. Magn. Reson. **172**, 296 (2005).
[50] R. S. Said and J. Twamley, Robust control of entanglement in a nitrogen-vacancy center coupled to a ^{13}C nuclear spin in diamond, Phys. Rev. A **80**, 032303 (2009).
[51] H. Y. Carr and E. M. Purcell, Effects of diffusion on free precession in nuclear magnetic resonance experiments, Phys. Rev. **94**, 630 (1954).
[52] S. Meiboom and D. Gill, Modified spin-echo method for measuring nuclear relaxation times, Rev. Sci. Instrum. **29**, 688 (1958).
[53] A. W. Cross, L. S. Bishop, S. Sheldon, P. D. Nation, and J. M. Gambetta, Validating quantum computers using randomized model circuits, Phys. Rev. A **100**, 032328 (2019).
[54] S. Wimperis, Broadband, narrowband, and passband composite pulses for use in advanced NMR experiments, J. Magn. Reson. Ser. A **109**, 221 (1994).
[55] H. K. Cummins, G. Llewellyn, and J. A. Jones, Tackling systematic errors in quantum logic gates with composite rotations, Phys. Rev. A **67**, 042308 (2003).
[56] M. Bando, T. Ichikawa, Y. Kondo, and M. Nakahara, Concatenated composite pulses compensating simultaneous systematic errors, J. Phys. Soc. Jpn. **82**, 014004 (2013).
[57] A. Paszke, S. Gross, F. Massa, A. Lerer, J. Bradbury, G. Chanan, T. Killeen, Z. Lin, N. Gimelshein, L. Antiga, and A. Desmaison, Pytorch: An imperative style, high-performance deep learning library. Advances in neural information processing systems, 32 (2019).
[58] D. C. Liu and J. Nocedal, On the limited memory bfgs method for large scale optimization, Math. Program. **45**, 503 (1989).
[59] M. J. Biercuk, A. C. Doherty, and H. Uys, Dynamical decoupling sequence construction as a filter-design problem, J. Phys. B: At. Mol. Opt. Phys. **44**, 154002 (2011).
[60] T. Hangleiter, P. Cerfontaine, and H. Bluhm, Filter-function formalism and software package to compute quantum processes of gate sequences for classical non-Markovian noise, Phys. Rev. Res. **3**, 043047 (2021).

[61] P. Cerfontaine, T. Hangleiter, and H. Bluhm, Filter functions for quantum processes under correlated noise, Phys. Rev. Lett. **127**, 170403 (2021).
[62] T. Hangleiter, I. Nha Minh Le, and J. D. Teske, "filter_functions". Zenodo (2024). https://doi.org/10.5281/zenodo.11192918.
[63] K. D. Jahnke, A. Sipahigil, J. M. Binder, M. W. Doherty, M. Metsch, L. J. Rogers, N. B. Manson, M. D. Lukin, and F. Jelezko, Electron–phonon processes of the silicon-vacancy centre in diamond, New J. Phys. **17**, 043011 (2015).
[64] N. Moll, P. Barkoutsos, L. S. Bishop, J. M. Chow, A. Cross, D. J. Egger, S. Filipp, A. Fuhrer, J. M. Gambetta, M. Ganzhorn, A. Kandala, A. Mezzacapo, P. Müller, W. Riess, G. Salis, J. Smolin, I. Tavernelli, and K. Temme, Quantum optimization using variational algorithms on near-term quantum devices, Quantum Sci. Technol. **3**, 030503 (2018).
[65] M. A. Nielsen and I. L. Chuang, *Quantum Computation and Quantum Information: 10th Anniversary Edition* (Cambridge University Press, Cambridge, 2010).
[66] C. T. Nguyen, D. D. Sukachev, M. K. Bhaskar, B. Machielse, D. S. Levonian, E. N. Knall, P. Stroganov, R. Riedinger, H. Park, M. Lončar, and M. D. Lukin, Quantum network nodes based on diamond qubits with an efficient nanophotonic interface, Phys. Rev. Lett. **123**, 183602 (2019).
[67] N. H. Wan, T.-J. Lu, K. C. Chen, M. P. Walsh, M. E. Trusheim, L. De Santis, E. A. Bersin, I. B. Harris, S. L. Mouradian, I. R. Christen, E. S. Bielejec, and D. Englund, Large-scale integration of artificial atoms in hybrid photonic circuits, Nature **583**, 226 (2020).
[68] B. Machielse, S. Bogdanovic, S. Meesala, S. Gauthier, M. J. Burek, G. Joe, M. Chalupnik, Y. I. Sohn, J. Holzgrafe, R. E. Evans, C. Chia, H. Atikian, M. K. Bhaskar, D. D. Sukachev, L. Shao, S. Maity, M. D. Lukin, and M. Lončar, Quantum interference of electromechanically stabilized emitters in nanophotonic devices, Phys. Rev. X **9**, 031022 (2019).
[69] P. Anand, L. Follet, O. Hooybergs, and D. Englund, SI_Programmable_Quantum_Matter_2025—Google Drive—drive.google.com, https://drive.google.com/drive/folders/1gqB1cdJpg_otDfSoiKS4JsFGrrLeY_Bv?usp=sharing, 2025.
[70] H. Raniwala, P. Anand, S. Krastanov, M. Eichenfield, M. Trusheim, and D. R. Englund, Spin-optomechanical cavity interfaces by deep subwavelength phonon-photon confinement, npj Quantum Inf. **11**, 120 (2025).
[71] T. Iwasaki, F. Ishibashi, Y. Miyamoto, Y. Doi, S. Kobayashi, T. Miyazaki, K. Tahara, K. D. Jahnke, L. J. Rogers, B. Naydenov *et al.*, Germanium-vacancy single color centers in diamond, Sci. Rep. **5**, 12882 (2015).
[72] M. Prabhu, C. Errando-Herranz, L. De Santis, I. Christen, C. Chen, C. Gerlach, and D. Englund, Individually addressable and spectrally programmable artificial atoms in silicon photonics, Nat. Commun. **14**, 2380 (2023).
[73] V. Saggio, C. Errando-Herranz, S. Gyger, C. Panuski, M. Prabhu, L. De Santis, I. Christen, D. Ornelas-Huerta, H. Raniwala, C. Gerlach, M. Colangelo, and D. Englund, Cavity-enhanced single artificial atoms in silicon, Nat. Commun. **15**, 5296 (2024).
[74] D. Dhaliah, Y. Xiong, A. Sipahigil, S. M. Griffin, and G. Hautier, First-principles study of the t center in silicon, Phys. Rev. Mater. **6**, L053201 (2022).
[75] A. Buzzi, C. Papon, M. Pirro, O. Hooybergs, H. Raniwala, V. Saggio, C. Errando-Herranz, and D. Englund, Spectral tuning and nanoscale localization of single color centers in silicon via controllable strain, Nat. Commun. **16**, 8829 (2025).
[76] S. Simmons, Scalable fault-tolerant quantum technologies with silicon color centers, PRX Quantum **5**, 010102 (2024).
[77] D. B. Higginbottom, F. K. Asadi, C. Chartrand, J.-W. Ji, L. Bergeron, M. L. Thewalt, C. Simon, and S. Simmons, Memory and transduction prospects for silicon *t* center devices, PRX Quantum **4**, 020308 (2023).
[78] E. Sörman, N. T. Son, W. M. Chen, O. Kordina, C. Hallin, and E. Janzén, Silicon vacancy related defect in 4h and 6h sic, Phys. Rev. B **61**, 2613 (2000).
[79] D. Louzon, G. T. Genov, N. Staudenmaier, F. Frank, J. Lang, M. L. Markham, A. Retzker, and F. Jelezko, Robust noise suppression and quantum sensing by continuous phased dynamical decoupling, Phys. Rev. Lett. **134**, 120802 (2025).
[80] A. Ulanowski, O. Kuijpers, B. Merkel, A. Holzäpfel, and A. Reiserer, Cavity-enhanced spectroscopy of individual nuclear spins in a dense bath, PRX Quantum **6**, 020344 (2025).
[81] P. Anand, E. G. Arnault, M. E. Trusheim, K. Jacobs, and D. R. Englund, Microwave single-photon detection using a hybrid spin-optomechanical quantum interface, npj Quantum Inf. **11**, 164 (2025).
[82] J. Johansson, P. Nation, and F. Nori, Qutip: An open-source Python framework for the dynamics of open quantum systems, Comput. Phys. Commun. **183**, 1760 (2012).
[83] J. Johansson, P. Nation, and F. Nori, Qutip 2: A Python framework for the dynamics of open quantum systems, Comput. Phys. Commun. **184**, 1234 (2013).
[84] N. Lambert, E. Giguère, P. Menczel, B. Li, P. Hopf, G. Suárez, M. Gali, J. Lishman, R. Gadhvi, R. Agarwal, and A. Galicia, QuTiP 5: The quantum toolbox in Python. Physics Reports, 2026, 1153, pp. 1–62.
[85] P. Anand, L. Follet, and O. Hooybergs, Codes, 2025, https://github.com/FolletLouis/Programmable-Quantum-Matter
[86] M. Mirhosseini, A. Sipahigil, M. Kalaee, and O. Painter, Superconducting qubit to optical photon transduction, Nature **588**, 599 (2020).
[87] Diamond Properties, https://www.chm.bris.ac.uk/motm/diamond/diamprop.htm.
[88] B. Mukherjee and A. Boyle, On the Debye characteristic temperature of diamond, Phys. Status Solidi (B) **22**, K131 (1967).
[89] J. F. Barry, J. M. Schloss, E. Bauch, M. J. Turner, C. A. Hart, L. M. Pham, and R. L. Walsworth, Sensitivity optimization for NV-diamond magnetometry, Rev. Mod. Phys. **92**, 015004 (2020).